

RESEARCH ARTICLE

10.1029/2018JC013876

Key Points:

- Concentrated benthic suspension (CBS) of mud in the turbidity maximum zone was observed by a comprehensive near-bed tripod system
- The dynamics for the formation of CBS are determined
- A one-dimensional vertical model is developed to analyze the physical mechanisms responsible for the formation of CBS

Correspondence to:

J. Ge,
jzge@sklec.ecnu.edu.cn

Citation:

Ge, J., Zhou, Z., Yang, W., Ding, P., Chen, C., Wang, Z. B., & Gu, J. (2018). Formation of concentrated benthic suspension in a time-dependent salt wedge estuary. *Journal of Geophysical Research: Oceans*, 123, 8581–8607. <https://doi.org/10.1029/2018JC013876>

Received 2 FEB 2018

Accepted 1 NOV 2018

Accepted article online 6 NOV 2018

Published online 27 NOV 2018

Formation of Concentrated Benthic Suspension in a Time-Dependent Salt Wedge Estuary

Jianzhong Ge^{1,2} , Zaiyang Zhou¹ , Wanlun Yang¹, Pingxing Ding^{1,2} , Changsheng Chen^{3,4} , Zheng Bing Wang^{5,6} , and Jinghua Gu¹ 

¹State Key Laboratory of Estuarine and Coastal Research, East China Normal University, Shanghai, China, ²Institute of Eco-Chongming, Shanghai, China, ³School of Marine Science and Technology, University of Massachusetts Dartmouth, New Bedford, MA, USA, ⁴International Center for Marine Studies, Shanghai Ocean University, Shanghai, China, ⁵Faculty of Civil Engineering and Geosciences, Delft University of Technology, Delft, The Netherlands, ⁶Deltares, Delft, The Netherlands

Abstract The concentrated benthic suspension (CBS) of mud, as a major contributor of sediment transport in the turbidity maximum of the estuary, is of great challenge to be correctly monitored through field measurements, and its formation mechanism is not well understood. A tripod system equipped with multiple instruments was deployed to measure the near-bed hydrodynamics and sediments in the North Passage of the Changjiang Estuary, with the aim at determining the formation mechanisms of CBS. The measurements detected a significant dominance of high sediment concentration in the near-bed 1-m layer: ~20 g/L at the southern site and ~47 g/L at the northern site. Strong CBS occurred under weak tidal mixing condition and was directly relevant to the sediment-induced suppression of turbulent kinetic energy and the enhanced water stratification due to saltwater intrusion and sediment suspension. During the weak-mixing neap period, the typical thickness of CBS was about 0.2–0.3 m, with a life time of ~2.83 hr (suspended-sediment concentration > 15.0 g/L). Enhanced water stratification reduced vertical mixing and confined the sediment entrainment from the near-bed layer to the upper column. This enhancement was due to the suppression of turbulent kinetic energy as a result of the sediment accumulation in the near-bottom column during the slack water and also due to the appearance of a two-layer salinity structure in the vertical as a result of saltwater intrusion near the bottom. These physical processes worked as a positive feedback loop during the formation of CBS and can be simulated with a process-oriented, one-dimensional vertical CBS model.

Plain Language Summary In the turbidity maximum, concentrated benthic suspension (CBS) frequently dominates the near-bed sediment transport, which, however, is difficult to be correctly observed, especially in the stratified condition. And the formation mechanism of CBS is complex due to the interaction of sediment and hydrodynamics. In a stratified tide channel of the Changjiang Estuary, China, a comprehensive tripod system, integrated with many cutting-edge instruments, is developed and deployed to measure the CBS and to determine the formation process. This system detected the existence of CBS in the lower near-bed 1-m layer, ~20 g/L at the southern site and ~47 g/L at the northern site, with the mean thickness of 20–30 cm. The corresponding salinity, tidal velocities, wave, and turbulent kinetic energy were also recorded. During the formation of CBS, tidal mixing is weak. And the salinity/sediment-induced stratification greatly limits the vertical mixing and suppresses the turbulent kinetic energy production. The saltwater intrusion creates a two-layer structure of salinity, leading to stratification and decreasing the mixing. These physical effects work like a positive feedback loop. A one-dimensional vertical model had been developed to successfully simulate the formation process of CBS, indicating the stable CBS during weak-tidal-mixing neap cycle.

1. Introduction

Mud, a mixture of clay, silt, fine sand, and organic particles, is a major sediment type in the turbidity maximum zone of an estuary. The turbidity maximum zone is an area where a river with abundant sediment and freshwater discharge is connected to a sea or an ocean. It is a gateway for sand and mud from the terrestrial source to sink in the marine environment. The mud suspension in the turbidity maximum zone produces a significant mass exchange between the water column and seabed, which can have great impacts on hydrodynamics, morphological development, ecosystem, and biogeochemistry at either local

or regional scale (Ge et al., 2015a; Geyer & MacCready, 2014; Toubanc et al., 2015; Winterwerp, 1999; Winterwerp & Van Kesteren, 2004). The concentrated benthic suspension (CBS) of mud can frequently occur around an estuary as a result of sediment deposition, mass or bulk erosion, and convergence under physical mechanisms (Bruens et al., 2002; Sottolichio & Castaing, 1999; Winterwerp, 2002, 2011). The near-bed sediment dynamics is of great challenge to be correctly monitored through field measurements, requiring jointed efforts with various instruments, including optical, acoustic, and even directly sampling techniques (Manning et al., 2010; Manning & Dyer, 2007; Sottolichio et al., 2011; Traykovski et al., 2000, 2007). The near-bed CBS is considered an important contributor to bed stratigraphy, channel siltation, and morphology with responses to the sinking effects of remote terrestrial particles, local resuspension, and entrainment. CBS has been shown to be a major component of sediment transport (Bruens, 2003; Ge et al., 2015b; Van Maren et al., 2009).

According to the definition by Winterwerp (1999), the highly concentrated mud suspension represents the cohesive sediment within the concentration range from ~ 100 to $\sim 1,000$ mg/L. The mud suspension with a concentration order of ~ 10 – 100 g/L is categorized as fluid mud. In an estuarine region, sediment concentration varies with depth in a wide range from ~ 100 mg/L in the upper water column to ~ 10 g/L in the lower water column near the bottom. Even under such conditions, the turbidity water still behaves like Newtonian fluid. Therefore, in this study we consider the suspension with a concentration of ~ 15 g/L as the CBS, which mainly occurs in the bottom layer, especially within the near-bed layer.

Many studies have been carried out to understand the influences of CBS on the suppression of turbulent kinetic energy (TKE) production (Geyer, 1993; Toorman et al., 2002), the self-stratification via sediment diffusivity (Dutta et al., 2014; Winterwerp, 2006), and the settling velocity with hindered effects (Baldock et al., 2004; Cuthbertson et al., 2008). The entrainment process from the lower CBS layer to the upper clear water layer was mainly examined through flume experiments and process-oriented numerical simulations (Bruens et al., 2002, 2012; Kranenburg, 1994). These process-oriented models are a helpful tool to understand the dynamics involved in both field measurements and flume experiments. For example, Winterwerp (2011) used a one-dimensional vertical (1DV) point model to examine the turbulence-induced flocculation and sediment-induced buoyancy destruction in the Ems River.

The identification and measurements of CBS, particularly under an environment characterized by energetic interactions of river discharge, tidal currents, and surface waves, are of great challenge to study the formation process for the CBS in a complex estuarine system. Unlike a flume experiment conducted under manual/computer control, the actual CBS is not easy to be captured during a shipboard field survey, since the CBS varies significantly with time and in space. It requires reliable state-of-the-art instruments with capabilities of resolving high-resolution vertical profiles of sediment concentration, velocity, stratification, and turbidity.

To examine the formation dynamics of the CBS near the bed surface in a strongly river-tide-interacting estuary, we deployed a comprehensive tripod system with multiple high-resolution instruments in the turbidity maximum zone of the Changjiang River Estuary. The measurements captured the formation process of CBS over a tidal cycle with significant saltwater intrusion. A 1DV CBS model was configured using the updated version 4.0 of Finite-Volume Community Ocean Model (FVCOM) and was used to examine the mechanism that controlled the formation of CBS in the estuary.

This paper summarizes the major findings from our comprehensive observations and process-oriented 1DV model experiments. The paper is organized as follows. In section 2, the study site and designs of field measurements with a tripod system and anchored vessels are described. In section 3, the major findings from the field measurements are summarized, and the mechanism of CBS formation is discussed. In section 4, the process-oriented 1DV model is introduced, and the model simulation results are presented. Finally, conclusions and follow-up discussion are presented in section 5.

2. Study Sites and Designs of Field Measurements

The Changjiang River is a major terrestrial source of sending particulate matters into the inner shelf of the East China Sea (Figure 1a). In the last decade, although the Three Gorges Dam and other upstream dams have strong regulation effects on the sediment discharge from the river to the sea (Chen et al., 2004; Yang et al.,

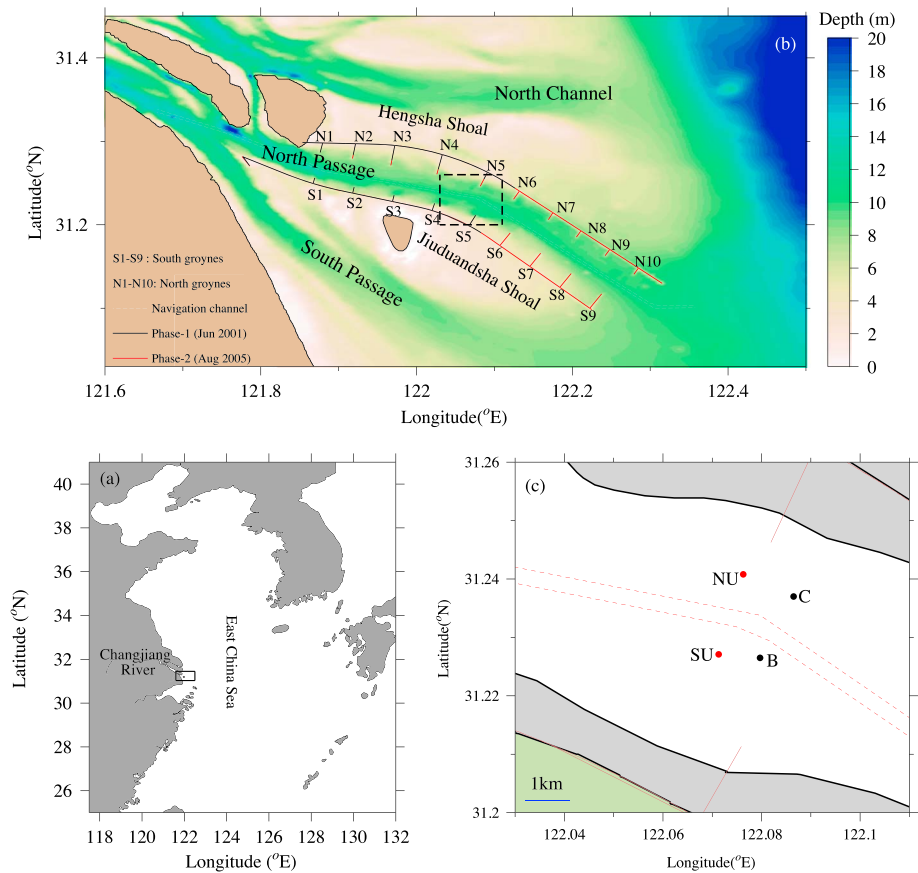


Figure 1. (a) Locations of the Changjiang River and the East China Sea. The small rectangle indicates the study area of the Changjiang Estuary, which is enlarged in Figure 1b. (b) The bathymetry of the Changjiang Estuary and the dikes and groynes along the North Passage. The small dashed box is the region for field observations, enlarged in Figure 1c. (c) Two tripod sites NU and SU and their nearby mooring stations B and C.

2011), the Changjiang River still carries an annual sediment load of $\sim 100\text{--}300$ Mt to the East China Sea (Luan et al., 2016). The sediment transport from the river has great impacts on shoreline evolution, island migration, channel generation, and subduction. It also forms one of the most remarkable turbidity maximum zones in the world.

Additionally, abundant freshwater discharge meets the saltwater from the ocean in the estuary, which creates a significant degree of stratification. The vertical mixing and stratification in the river estuary are under the effect of time-dependent salt wedge. Geyer and MacCready (2014) calculated the estuarine parameter space based on the freshwater Froude number and mixing number and classified the Changjiang River Estuary as a time-dependent salt wedge in a tidal-dominant estuary. Their estimation showed the tidal boundary layer had the possibility of reaching the sea surface in the Changjiang Estuary, indicating the tide could have a modulation effect on the stratification.

The remote sensing images of the surface sediment concentration, derived from the Geostational Ocean Color Imager satellite, clearly verified the nature of high turbidity of the Changjiang River (Ge et al., 2015b; Shen et al., 2013). The river mouth is a typical turbidity maximum zone, where the sediment concentration near the surface remains at $\sim 0.2\text{--}0.5$ g/L. The river mouth is also consisted as a channel-shoal system. The Jiuduansha Shoal and Hengsha Shoal split this estuary into three channels: the North Channel, the North Passage, and the South Passage (Figure 1b). Two parallel dikes and many perpendicular groynes were built along the North Passage, which were designed to increase the flow energy in the main channel and hence to reduce sediment siltation and deepen the channel (Ge et al., 2012; Pan et al., 2012). As the consequence of deepened channel, the dike-groyne construction has physically trapped the sediment and made the

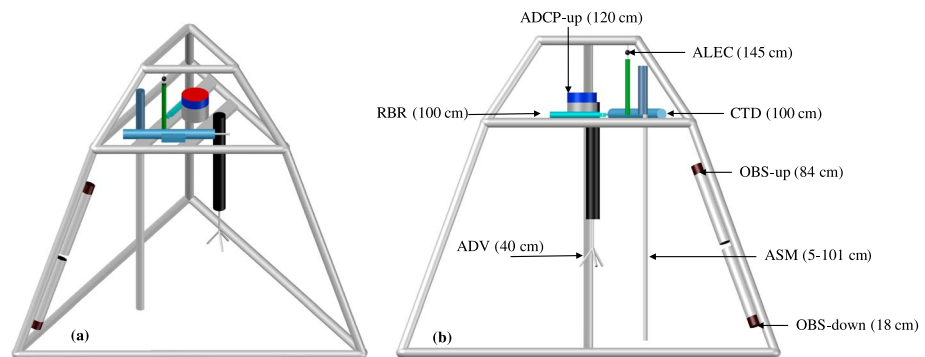


Figure 2. (a) Top view and (b) side view of the tripod system with acoustic Doppler current profiler (ADCP)-up, conductivity-temperature-depth (CTD), acoustic Doppler velocimetry (ADV), optical backscattering sensor (OBS)-up, OBS-down, RBR, ALEC, and Argus Surface Meter-IV (ASM). The heights (in centimeters above the bed) of these instruments are indicated.

North Passage the most energetic channel with significant variability of sediment concentration (Ge et al., 2012, 2015a, 2015b; Li et al., 2016; Pan et al., 2012).

Previous sediment studies in the Changjiang River mainly focused on diluted suspension (Hu et al., 2009; Jiang et al., 2013; Li & Zhang, 1998; Li et al., 2016; Shen & Verhoef, 2010; Song et al., 2013). Some near-bed measurements were made to examine benthic processes (Song et al., 2013), but only a few were successful at identifying the CBS with a concentration reaching ~ 20 g/L in the central North Passage (Liu et al., 2011), without explaining the mechanisms of its formation and breakdown.

The North Passage was selected to be the study site for the field monitoring (Figure 1). This region is defined as a turbidity maximum zone with strong interaction of tidal currents and river discharge based on previous measurements (Liu et al., 2011). The previous field measurements (see Figures 16 and 17 in Ge et al., 2013) showed that in the North Passage the water is periodically stratified, with a significant surface-bottom salinity difference (~ 15 practical salinity unit [PSU]) during the late-flooding phase and a well-mixed water column during the late-ebb phase. This pattern agrees well with the classification of time-dependent salt wedges discussed in Geyer and MacCready (2014).

We equipped two tripod systems with multiple state-of-the-art instruments. Each tripod system was designed as a half-pyramid shape with a two-layer structure (Figure 2). On the upper layer, an upward-looking acoustic Doppler current profiler (ADCP-up) was mounted at 1.20 m above the bed (hereafter referred to as “mab”); a current meter (ALEC Infinity-electromagnetic (EM) current meter; JFE Advantech Co., Ltd.) at 1.45 mab to acquire the current data in the blindness of the ADCP-up; a tide/wave logger (RBRduo) at 1.0 mab to record the fluctuation of the sea surface; and a Conductivity-Temperature-Depth (CTD) at the same 1.0 mab to record temperature and salinity. The lower layer had 1.0-m height. Two tail-connected optical backscattering sensors (type: OBS-3A, D&A Instruments) were mounted on the side ridge of the lower pyramid and had the sensor heights of OBS-down at 0.18 mab and of OBS-up at 0.84 mab. A Nortek acoustic Doppler velocimetry (ADV) instrument was installed at the middle of the pyramid to avoid ridge’s influence on water’s fluctuations. The sensor position was at 0.4 mab, which qualified the valid data coming from ~ 0.25 mab. Particularly, a high-resolution Argus Surface Meter-IV (ASM) was positioned at a corner of the pyramid, which covered the range of 0.05–1.01 mab. This ASM had a total of 96 optical sensors and 1-cm spatial interval along the rod, which was designed to record turbidity variation in the whole 96-cm profile. Detailed configuration of all these sensors, such as average sampling resolution, duration, and frequency, are listed in Table 1. Two tripod systems were deployed at two sites labeled NU and SU in Figure 1c. The mean water depths at NU and SU were 10 and 11 m, respectively. Sites NU and SU were selected with the consideration of instrument protection from possible damages due to the busiest navigation in the North Passage. Additionally, two mooring vessels were anchored at two sites labeled B and C in Figure 1c. Sites B and C were very close to sites NU and SU, and the anchored vessels were used to monitor the diluted suspension layer above the tripod. The measurements were conducted over a 15-day period from 20 July to 3 August 2015, which covered a full spring-neap cycle. During this period, the average freshwater discharge from the upstream Changjiang River was $\sim 46,000$ m³/s.

Table 1
Configurations for the Instruments Installed on the Tripod System

Instrument deployed	Distance above bed (m)	Sampling interval (min)	Sampling configuration	Survey parameter
Acoustic Doppler current profilers	1.2 (upward)	2	Cell size: 0.5 m	Profile velocity
Acoustic Doppler vector(Nortek)	0.25	10	16 Hz * 70 s	Near-bed velocity
Argus Surface Meter-I	0.05–1.01	2		SSC
RBRduo Tide &Wave Loggers	1	10		Wave conditions
ALEC Infinity-EM	1.45	2	0.2 Hz * 50 s	Velocity
OBS-3A	0.840.18	22		Salinity, temperature, SSC Salinity, temperature, SSC

Note. EM = electromagnetic; OBS = optical backscattering sensor; SSC = suspended-sediment concentration.

3. Data and Identification of CBS

The OBS-3A and ASM were optical sensors that measured water turbidity in nephelometric turbidity units (NTU). Sediment samples were collected during the survey period at the tripod sites and put in a standard rotating water tank at our laboratory. These samples were used to calibrate the sensors by constructing the regression function of water turbidity with suspended-sediment concentration (SSC) at each tripod site. The calibrated results showed different regression patterns of water turbidity via the sediment concentrations for ASM and OBS-3A at sites SU and NU. For ASM, a piecewise regression function was found at site SU, featuring a linear straight line when turbidity <500 NTU and a third-order polynomial fitting curvature line when turbidity >500 NTU (Table 2). At site NU, the relationship between turbidity and SSC was fitted well with a third-order polynomial line in the whole range of turbidity measurements. For OBS-3A, at both sites SU and NU, the relationship between turbidity and SSC was presented by a piecewise regression function, similar to that for ASM at site SU. The regression equations for AMS and OBS-3A are given in Table 2, in which the value of R^2 (>0.95) indicates a reliable fitting above the 95% confidence level. Using these regression functions, we converted the water turbidity recorded by ASM and OBS to SSC in the units of gram per liter.

The time series recorded by the multiple sensors provided us insights of the variability of SSC and related physical components over a spring-neap tidal cycle. This is highlighted in Figure 3, including the time series of tidal elevation, water velocity, significant wave height, salinity, TKE, and SSC at sites SU and NU. The SSC varied over the tidal cycle, with a peak value at the time of the minimum tidal flow during the flood-to-ebb transition. Even though both sites SU and NU were close to each other in the North Passage, the variability of SSC differed significantly at both sites, on both short-term (semidaily) and long-term (neap-spring cycle) scales.

At site SU, SSC was relatively low during the neap tidal cycle of 24–27 July (see the shaded area in Figure 3), with an average value of 1.98 g/L at 0.18 mab and of 0.76 g/L at 0.84 mab; and it was high during the spring tidal cycle of 31 July to 3 August, with an average value of 7.21 g/L at 0.18 mab and of 2.77 g/L at 0.84 mab. At this site, the CBS mainly occurred during the spring tidal cycle, with a maximum SSC of 20.98 g/L at the time

Table 2
Regression Between Optically Sensed Turbidity and Suspended-Sediment Concentration

Instruments	Results of calibration	R^2
SU: ASM	$y_1 = 1.2 * 10^{-3}x + 6.7 * 10^{-2}$ ($0 < x < 500$) $y_2 = 1.0 * 10^{-9}x^3 - 2.2 * 10^{-6}x^2 + 2. * 10^{-3}x - 0.3$ ($500 \leq x \leq 4000$)	0.995 0.999
NU: ASM	$y = 1.2 * 10^{-10}x^3 + 5.2 * 10^{-7}x^2 + 3.7 * 10^{-4}x + 0.38$ ($0 \leq x \leq 4000$)	0.990
SU: OBS (down)	$y_1 = 1.4 * 10^{-3}x - 3.3 * 10^{-2}$ ($0 < x < 500$) $y_2 = 7.6 * 10^{-10}x^3 - 3.4 * 10^{-6}x^2 + 6.7 * 10^{-3}x - 1.9$ ($500 \leq x \leq 4000$)	0.954 0.987
NU: OBS (down)	$y_1 = 1.7 * 10^{-3}x + 0.43$ ($0 < x < 500$) $y_2 = 2.5 * 10^{-9}x^3 - 8.8 * 10^{-6}x^2 + 1.2 * 10^{-2}x - 3$ ($500 \leq x \leq 4000$)	0.977 0.991

Note. The variables of x and y_1/y_2 indicate the optically sensed turbidity and corresponding calibrated sediment concentration, respectively. ASM = Argus Surface Meter-IV; OBS = optical backscattering sensor.

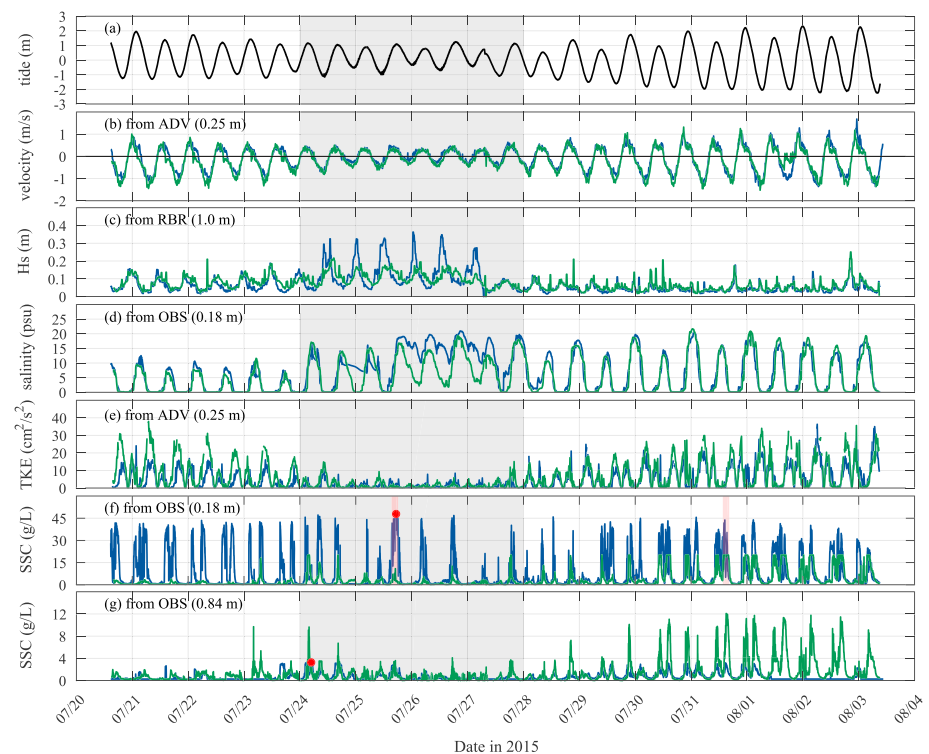


Figure 3. Time series of tide elevation, horizontal velocity from acoustic Doppler velocimetry (ADV; 0.25 mab), significant wave height from RBR, salinity from optical backscattering sensor (OBS)-down (0.18 mab), derived turbulent kinetic energy (TKE) from ADV, suspended-sediment concentration (SSC) from OBS-down (0.18 mab), and SSC from OBS-up (0.84 mab) at NU (blue) and SU (green) tripod sites. The shaded region indicates the neap tidal period.

of the maximum tidal current during the semidiurnal tidal cycles. Even at 0.84 mab, the CBS exhibited a similar pattern as that at 0.18 mab, with a peak SSC of 12.07 g/L at 15:04 local standard time (LST) on 31 July. Note that the flatness of SSC peaks was mainly caused by the limited measuring range of the OBS. During the neap tidal cycle, the CBS suddenly formed a sharp peak over a short time period, with the maximum SSC up to ~18 g/L at 0.18 mab.

At site NU, different patterns of CBS emerged. At 0.18 mab, timing and frequency of CBS occurrence remained the same over all tidal cycles. The maximum concentration of the mud suspension was 47.54 g/L, which occurred at 17:32 LST on July 25 during the neap cycle. Most of these SSC peaks had a value >30 g/L (Figure 3f), demonstrating that site NU was featured by a strong dominance of CBS. Unlike site SU, the SSC at site NU decreased significantly in a short distance away from the seabed. At 0.84 mab, the SSC dropped to ~1.0 g/L, with the maximum value of 3.18 g/L that occurred at 05:04 LST on July 24 during the neap tidal cycle (Figure 3g).

The statistics regarding the occurrence of CBS at sites NU and SU over the entire measurement period were analyzed, and our key findings are illustrated in Figure 4. The CBS was a common feature for the suspended sediment in the North Passage. At site NU, the CBS occurred with a frequency of 20.7%, the maximum SSC of 47.54 g/L, and the longest duration of 2.83 hr. Strong CBS was found during the neap tidal cycle. At site SU, although the mud suspension remained at a lower concentration and CBS occurred with a frequency of only 7.74%, it showed its longest duration of ~2.73 hr (Figure 4b), which occurred during the spring tidal cycle. This suggests that the CBS was an important contributor to the benthic sediment transport at these sites.

4. Formation and Breakdown Mechanisms of CBS

The tripod measurements showed the strong tidal variations of currents, salinity, and sediment transport as well as the variation of vertical mixing at both sites during the neap-spring cycle. The Changjiang Estuary is a tidal-dominated regime. The variations caused by tidal mixing and stratification play critical roles in sediment

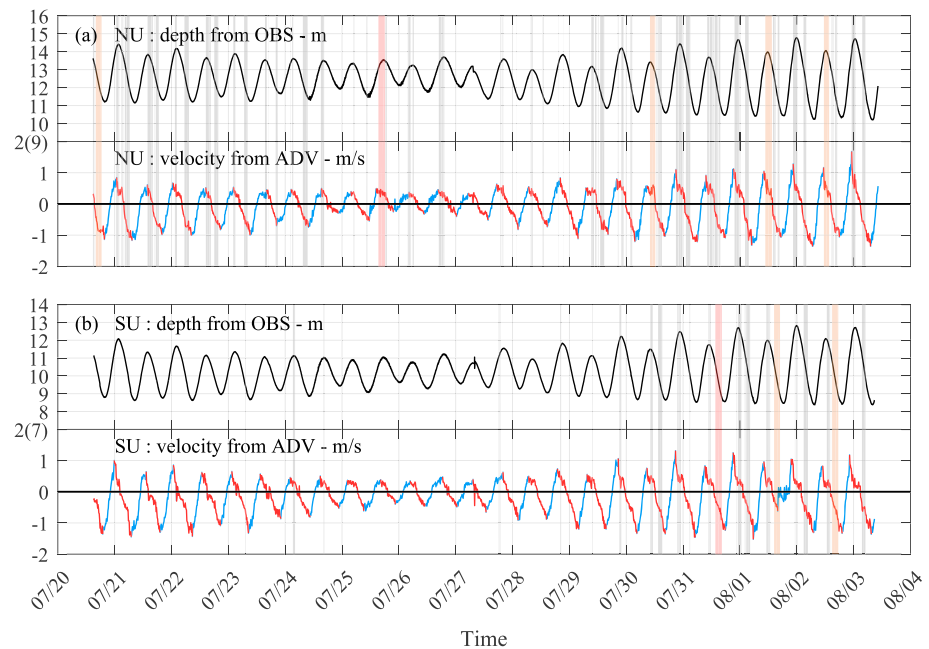


Figure 4. Time series of depth from optical backscattering sensor (OBS) and velocity from acoustic Doppler velocimetry (ADV) at sites (a) NU and (b) SU. The pink shading demonstrates the longest occurrence of concentrated benthic suspension (CBS) at these two tripod sites. The yellow shading indicates the occurrence of CBS longer than 2 hr; the gray shading shows the occurrence of CBS shorter than 2 hr. The red line in the velocity plot indicates the late-flood to early-ebb period, and the blue line indicates the late-ebb to early-flood period.

transport, particularly in the formation and breakdown of the CBS. In addition, the sediment has an impact on the physics of the water column. The sediment-induced density gradient can change the stratification and thus the baroclinic pressure gradient force. These processes are described and discussed next.

4.1. Tidal Mixing

In the North Passage, tidal-induced shear is a major force that caused the sediment to be eroded away from consolidated seabed, resuspended from the unconsolidated bed load and entrained from fluid mud or CBS (Song et al., 2013). It also plays an important role in sediment deposition and accumulation in the benthic layer when either current was weak or water was stratified.

The tripod measurements clearly show that the occurrence of the CBS was highly correlated with the tidal phase, mainly taking place in the late-flood to early-ebb period (Figure 4). In view of tidal elevation, the CBS frequently took place at high water or during the high-to-low transition period. During the rising period of tidal elevation, no evidence of CBS was observed at either site. The CBS mainly occurred during the late-flood or early-ebb period. Figure 5 shows that the CBS had a high probability of occurrence during the transition period from the flood tide to the ebb tide and was not able to form during the late-ebb or early-flood period. These results demonstrate that the tidal currents and tidal-induced mixing had significant influences on the formation of CBS.

Many studies used the Simpson number (Burchard et al., 2011; Stacey et al., 2010) to estimate the intensity of tidal mixing. The Simpson number is defined as the ratio of the potential energy change due to tidal straining to the production rate of TKE. However, the Simpson number only applies to the case with availability of horizontal gradients of density and tidal velocity. The Simpson number is also known as the horizontal Richardson number, which is not suitable for our case. Burchard et al. (2011) defined an unsteadiness number to estimate the efficiency of tidal mixing based on the ratio of water depth to friction velocity for a given tidal frequency. However, it applies only to the estuarine in the absence of stratification. Therefore, it is not applicable for our case since the Changjiang River and inner shelf of the East China Sea were well stratified during the measurement period (Chen et al., 2008; Ge et al., 2012, 2015). Geyer and MacCready (2014) proposed a mixing parameter to quantify the effectiveness of tidal mixing for the stratified estuary as follows:

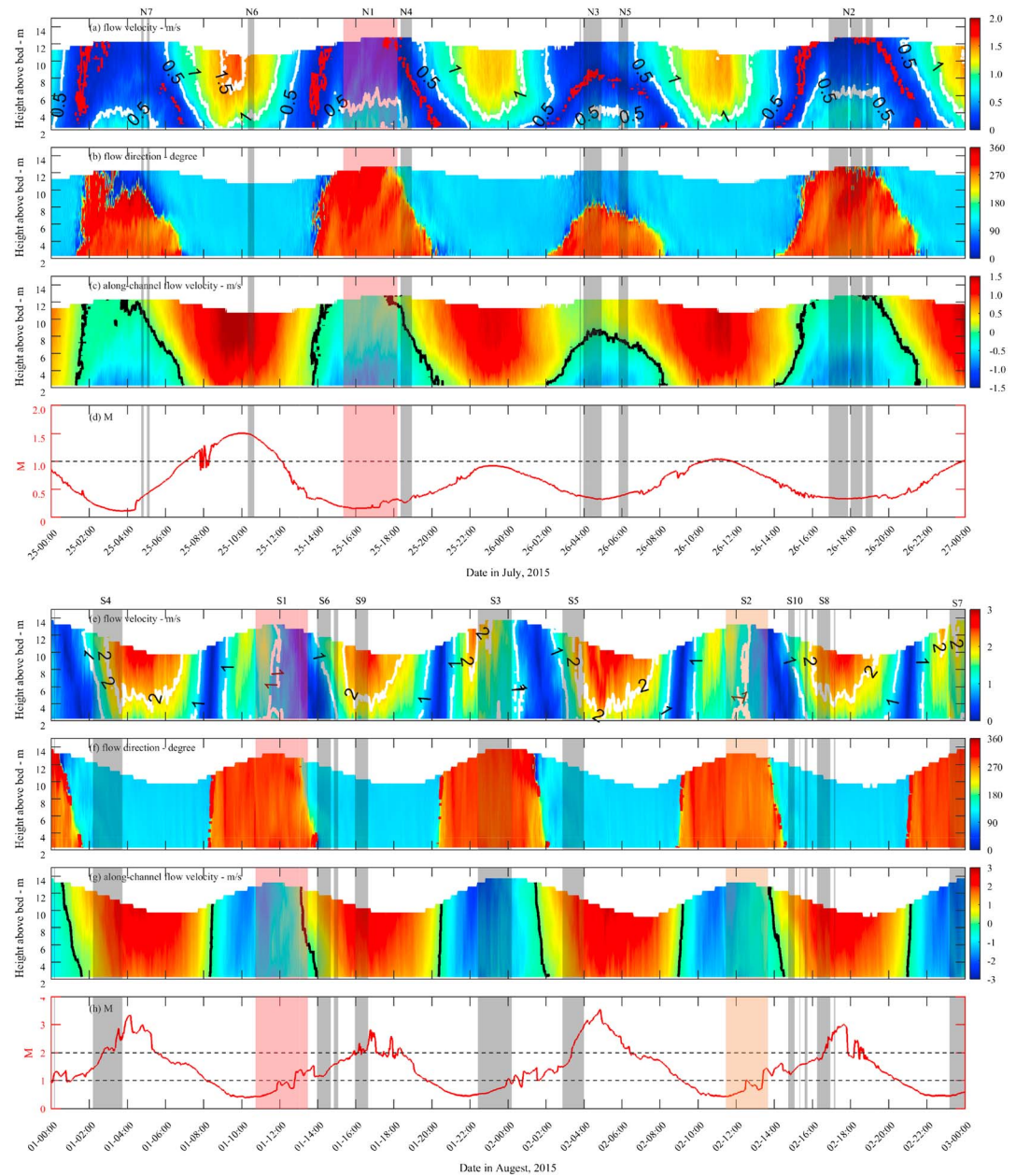


Figure 5. Time series of vertical profiles of (a) flow velocity, (b) flow direction, (c) along-channel flow velocity, and (d) mixing effectiveness parameter during neap tide at site NU. (e–h) Same as Figures 5a–5d, except during spring tide. The shaded regions with labels N1–N7 show the occurrences of concentrated benthic suspension during neap tide, and those with labels S1–S10 indicate the occurrences of concentrated benthic suspension during spring tide.

$$M^2 = \frac{C_d U_T^2}{\omega N H^2}, \quad (1)$$

where $N = \sqrt{\frac{\beta g S_{\text{ocean}}}{H}}$ is the buoyancy frequency, U_T is the magnitude of tidal velocity, H is the water depth, C_d is a constant parameter, ω is tidal frequency, and S_{ocean} is the reference salinity (Geyer, 2010; Geyer & Ralston, 2011). It is set as the mean salinity out of the estuary during the summer time (with a constant value of 30.0 psu; Ge et al., 2013), and g is gradational acceleration taken as a constant of $9.8 \text{ m}^2/\text{s}$. In Geyer and MacCready (2014), a constant $\beta = 7.7 \times 10^{-4}$ was specified. In the Changjiang estuary, the actual density ρ can change rapidly due to varying salinity. Instead of using a constant, $\beta = \left(\frac{\rho}{\rho_0} - 1\right)/s$ is used to

determine the time series buoyancy frequency, where s is the instantaneous salinity at the time when β is calculated. Tidal mixing is defined to be effective when $M > 2.0$, when well-mixed water column is produced (Geyer & MacCready, 2014).

Applying equation (1), we estimated M at sites NU and SU. In the North Passage, the M_2 tide dominated, so the estimation was made for the M_2 tidal frequency. In our calculation, U_T was determined by moving average of U_H over the $T/2$ tidal period (T was the M_2 tidal period), and U_H was the mean vertical velocity derived from the ADCP records. N was calculated using the salinity recorded on the tripods and by the nearby anchored vessels over the same $T/2$ tidal period. H was determined by moving average of water depth measured by OBS (down) mounted on the tripods over the $T/2$ tidal period. C_d was taken as 0.0025. Therefore, the U_T , N_0 , and H in equation (1) are all time dependent on the tide and degree of stratification during the calculation of M .

The time series of tidal velocity, direction, and M at site NU over the neap and spring cycles are shown in Figure 5. The result of $M < 2.0$ during the neap cycles suggests that vertical tidal mixing was weak. The occurrence of CBS matched the low trough (<0.5) duration of M , implying that the vertical tidal mixing was suppressed during the weak tidal straining period. Considering M was estimated based on the magnitude of averaged tidal velocity in the $T/2$ tidal period, the instantaneous mixing efficiency should be much lower at the late-flood or early-ebb phase. In our case, the low value of M during the neap tidal cycle was a result of enhanced stratification due to the formation of a stable two-layer system in the vertical. A similar situation was found during the spring tidal cycle. M reached the highest value of >3.0 at the maximum ebb tidal current and the lowest value of <2.0 during the late-flood tidal period. This means the tripod site was vertically well mixed at the maximum ebb tide. The fact that the CBS occurred during the spring tidal period in which M was in the range from 0.5 to 2.0 suggested that the occurrence of CBS co-occurred with significantly weak tidal mixing. In our observations, we found that the CBS had a low probability to form when $M > 2.0$ over the spring-to-neap transition period.

Effectiveness of tidal mixing was also visible through the vertical distribution of velocity. The occurrences of CBS during the late-flood tidal phase, such as N4, N3, N5, and N7, were accompanied by a two-layer composition of water velocity. An opposite phase was observed for the tidal velocity in the vertical. When the upper water column was in the ebb tidal phase with a flow direction of $\sim 120^\circ$, the lower water column was in the flood tidal phase with a flow direction of $\sim 300^\circ$ (Figure 5c).

Note that during the increasing phase of M , the CBS events sometimes occurred after the lowest value of M (Figure 5). The M shown in Figure 5 is not the instantaneous mixing efficiency. Based on the definition of M , it is determined through the tidal velocity averaged over the $T/2$ tidal period. Therefore, the calculation of M was done by an integration over this period using the moving average method. Additionally, the CBS was not instantaneously formed when M reached its minimum. It requires the time for the sediments to accumulate into the CBS during their settling into the benthic layer. These two factors led to a delay of CBS formation with respect to the minimum M .

Both observations and model results also revealed that the threshold of M for the CBS formation differed between spring and neap tide cycles. During the neap tide, the CBS formed in the range of $M=0.5-1.0$, while during the spring tide, it was in the range of 1.0–2.0. This difference was mainly associated with the suspended-sediment load and typical sediment grain size in the upper water column, which were both much bigger during the spring tide than during the neap tide. The suspension contained larger-grain-size sediment particulate during the spring tide than during the neap cycle. Although the mixing efficiency was relatively larger during the spring tide, the settling of the larger-grain-size sediment was significant and adequate to form a CBS. To produce the CBS, the smaller-grain-size sediment suspension during the neap cycle could be easier to accumulate in the benthic layer under weak mixing condition with smaller M .

In summary, the measurements at the tripod sites clearly showed that weak tidal mixing and two-layer-structured tidal currents during the neap tidal cycle were the major contributors to the formation of CBS in the North Passage. During the CBS formation period, the tidal kinetic energy was insufficient to bring the sediment up from the seabed boundary to the upper water column. In this case, the downward sediment settling overcame the upward mixing, which induced bottom accumulation of sediment. When the two-layer structure of tidal currents was weakened during the spring tidal cycle, the weak tidal mixing during the

late-flood tidal phase could still lead to significant sediment settling into the lower column and to generate the CBS like what we observed at S1, S2, S3, and S7.

4.2. Turbulence Suppression

The ADV with the sensor depth at 0.4 mab was configured with a 16-Hz sampling frequency and for the 70-s continuous sampling period. The averaging interval for every burst sampling was 10 min (Table 1). u' , v' , and w' , denoting the quasinormal probabilities, are the x (east–west), y (south–north), and z (vertical) fluctuating components of the instantaneous velocity. The covariance $\overline{(u')^2}$, $\overline{(v')^2}$, and $\overline{(w')^2}$ present the mean turbulence normal stresses. TKE can be defined as in Tennekes and Lumley (1972):

$$k = \frac{1}{2} \left(\overline{(u')^2} + \overline{(v')^2} + \overline{(w')^2} \right). \quad (2)$$

This is the formula used to estimate TKE at sites SU and NU shown in Figure 3.

With similar magnitudes of the near-bed tide velocity at sites SU and NU (Figure 3b), we found that the TKE differed significantly during the tidal transition cycle of 20–24 July before the neap tidal cycle. During that period, the peaks of TKE's fluctuation at site SU were nearly 2 times as large as those at site NU. However, the magnitude of SSC at site NU was 1 order of magnitude larger than that at site SU. The near-bed TKE also reflected potential mixing from the bottom to the surface. Under a weak TKE condition, the sediment was confined in the lower water column. In this case, the water's mixing energy was too weak to produce an adequate transport in the upward direction.

During the neap tidal period, the tidal velocity and mixing were weak. The tidal energy was not capable of fully penetrating into the near-bed layer. Therefore, the TKE was remarkably low during this period, hence producing a sediment-settling-favorable condition. With small TKE, the bottom shear stress was not sufficient to cause significant erosion from the seabed; so the settling effect became dominant. Considering that the fine clay was the major component in sediment suspension and had a low consolidation rate, it mainly stayed in the near-bed layer to form a fluffy CBS layer. It was also easily resuspended into the water column through the entrainment by sufficient tidal mixing at the maximum ebb or flood tide.

After the neap tidal cycle, the TKE at site SU was still larger than that at site NU, but the difference in magnitude was smaller than that before the neap tidal cycle. This matched the reduced SSC difference between sites NU and SU during the spring tidal cycle. In general, lower TKE increased the sediment settling from the upper to lower column and decreased the sediment entrainment from the lower to upper column, which tended to cause significant sediment accumulation in the near-bed layer.

The observations, on the other hand, suggested that the high SSC in the near-bed layer also had negative feedback on the production rate of TKE as a result of the reduction of TKE and of diffusivity K by suspended sediment. A Richardson number-dependent formulation of K was derived by Munk and Anderson (1948), which is given here:

$$K = K_0 \left(1 + \frac{10}{3} Ri \right)^{-1.5}, \quad (3)$$

where K_0 is the constant diffusivity for well-mixed water and Ri is the gradient Richardson number defined as $Ri = -\frac{g}{\rho_w} \frac{\partial \rho / \partial z}{(\partial u / \partial z)^2}$, where ρ_w is the water density with consideration of pressure, salinity, temperature, and mud suspension. Using equation (3), we estimated the reduction of K using our measurements and obtained $K/K_0 = 0.018$ – 0.027 . The results showed that under a high near-bed SSC condition, as Ri increased, K decreased, which potentially suppressed the production rate of TKE. This process was closely related to stratification, which was physically caused by salt wedge or mud suspension. It should be mentioned that Ri is also an alternative for quantifying the amount of tidal mixing under stratified condition.

4.3. Salinity-Induced Stratification

The enhanced stratification characterized by the two-layer salinity structure was the result of freshwater discharge from the upstream of the Changjiang River and saltwater intrusion from the inner shelf of the East China Sea. This unique two-layer structure was clearly revealed by the salinity and current measurements on the anchored vessels at sites B and C, and shown in Figures 6 and 7, respectively. The maximum

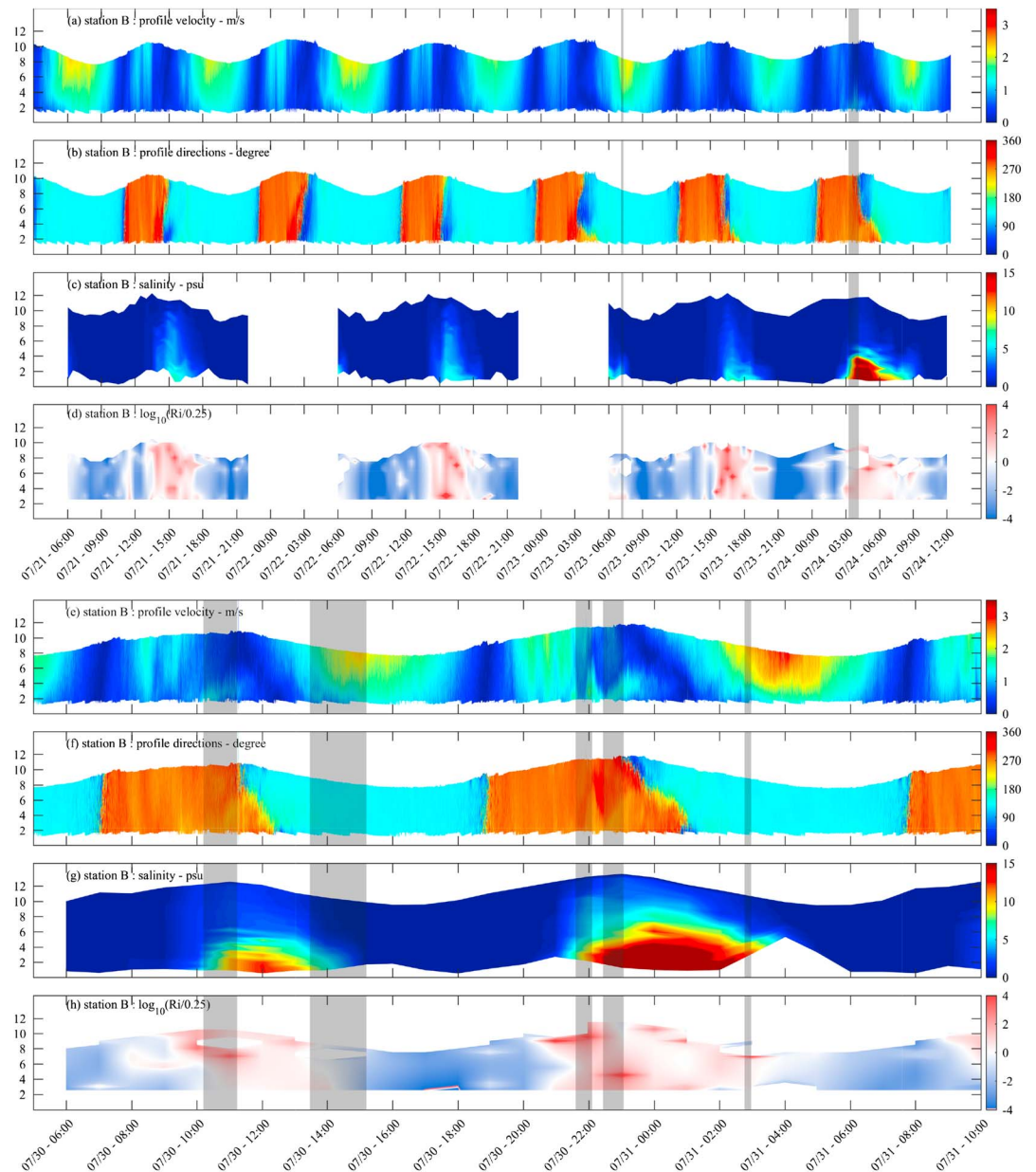


Figure 6. Time series of vertical profiles of (a) flow velocity, (b) flow direction, (c) salinity, and (d) log-scaled gradient Richardson number at mooring B during neap tide. (e–h) Same as Figures 6a–6d, except during spring tide. The shaded regions indicate the occurrences of concentrated benthic suspension at site SU.

vertical difference of salinity and velocity occurred during the transition period from the flood tide to the ebb tide. During that period, the upper layer featured a low-salinity offshore flow, while the lower layer showed a high-salinity onshore flow (Figures 6b, 6c, 7b, and 7c). The surface salinity remained at a low value of 0–2.0 psu during the spring and neap cycles. The maximum salinity near the bottom reached 20.0 psu when the strong saltwater intrusion occurred. The vertical distribution of the high-salinity water also exhibited different patterns during the neap and spring tidal cycles. During the neap tidal cycle, the high-salinity water stayed in the near-bed 4–6 mab when the strong stratification appeared (Figures 6c and 7c). During the spring tidal cycle, as the tidal mixing intensified, the high-salinity water was entrained into the upper water column, so that the thickness of the high-salinity water reached ~8 mab at site C and ~10 mab at site B. At site B, the high-salinity water mixed upward toward the surface at 00:00 LST on 31 July. Using $\log_{10}(Ri/0.25)$ as an index for stratification intensity, we found that the CBS co-occurred with strong

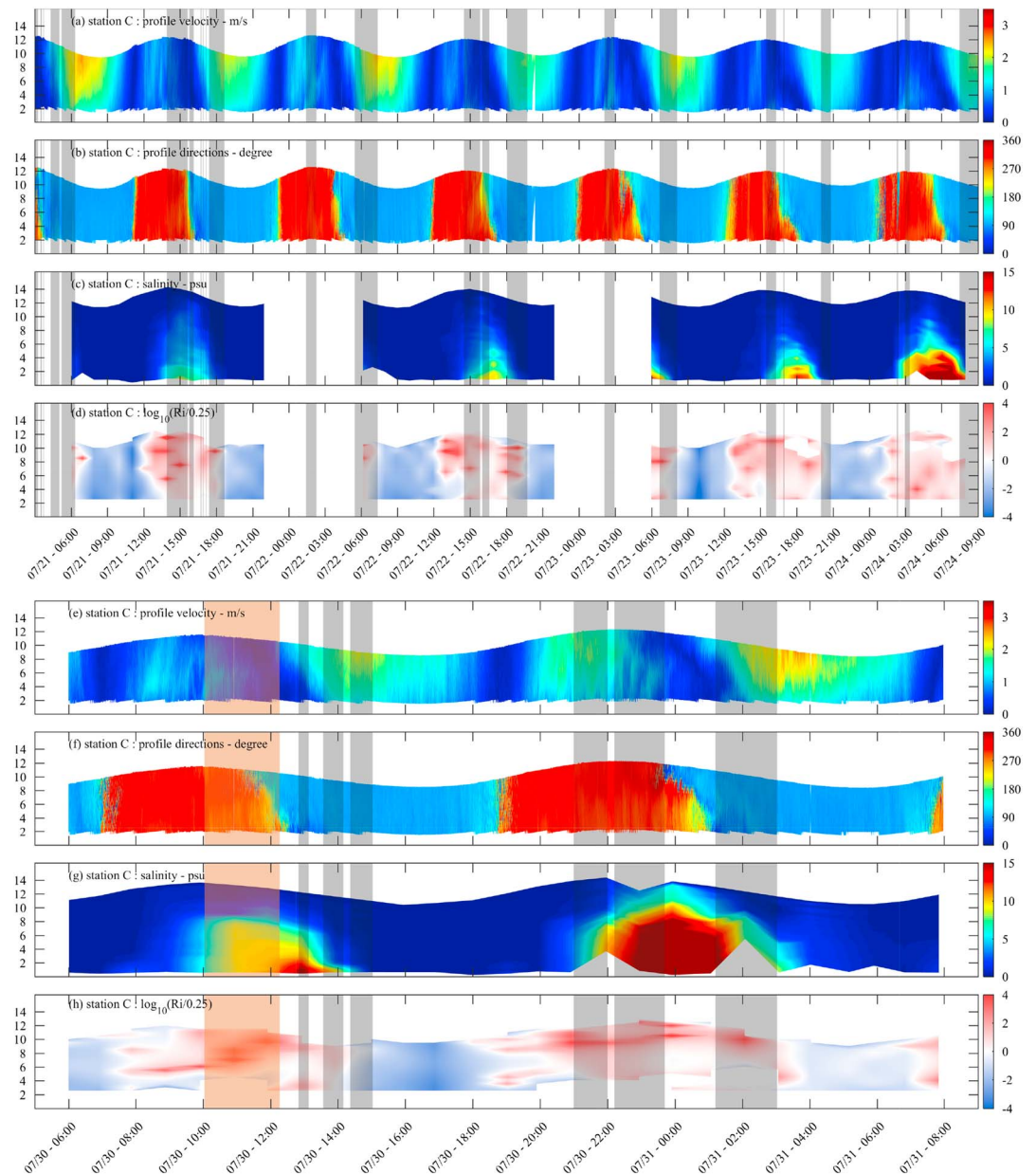


Figure 7. Same as Figure 6, except at site NU.

stratification during both spring and neap tidal cycles (Figure 7d). At site SU, for example, the CBS occurred during 10:00–12:00 LST on 30 July, during 21:00 LST on 30 July, and during 02:00 LST on 31 July.

During the strong saltwater intrusion period, the typical value of Ri ranged from 2.5 to 50, yielding a reduction of diffusivity by 2 orders of magnitude, based on equation (3) in Munk and Anderson (1948). It indicated significant suppression on the TKE production, which greatly limited the vertical mixing of sediment particles from the lower to upper water column.

4.4. Sediment-Induced Stratification

Here sediment-induced stratification referred to the stratification influenced by vertical gradient of the sediment density in the benthic bottom layer above the seabed. The SSC profiles within the 1-m-thick benthic layer were measured at a 1-cm resolution by the ASM (Figure 8). The whole water column in the 1-m benthic layer was covered by the high sediment suspension with an up-limit concentration of 20 g/L at site NU and of

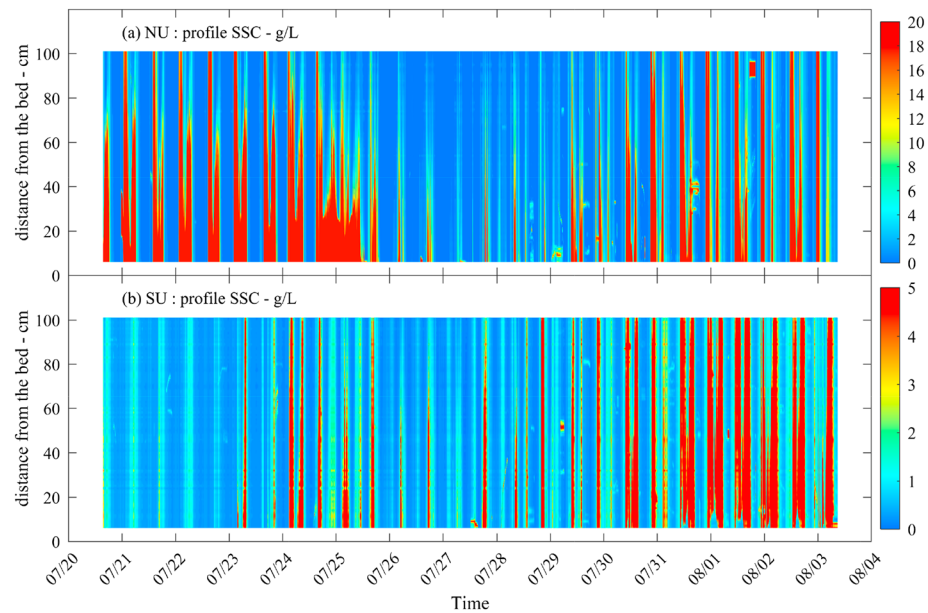


Figure 8. Variation of suspended-sediment concentration (SSC) in the near-bed 1-m range at sites (a) NU and (b) SU.

5 g/L at site SU. At site NU, the thickness of CBS was ~60–100 cm during the tidal transition period of 20–23 July. During the neap tidal cycle with the strong salinity-induced stratification and weak tidal mixing, the thickness of CBS decreased, and the vertical gradient of SSC increased in the bottom benthic layer. The upper 0.6- to 1.0-mab column was occupied by the sediment with a low concentration of <8 g/L, while the lower 0- to 0.4-mab column was featured by the continuous CBS accumulation. With this high-resolution AMS profiler, the nearly 1-day-lasting CBS was captured around 25 July at site NU (Figure 8a). During the neap tidal cycle of 26–28 July, the bottom benthic layer was occupied mainly by lower-concentration sediment except for some short-lived high-SSC events, which were identical to the OBS measurements. During the neap-to-spring transition period when the short-lived high-SSC events occurred, the thickness of CBS increased from 0.4 to 1.0 mab.

At site NU during the spring tidal cycle, the duration of short-lived high-SSC events gradually became longer as the tidal velocity increased. At site SU, the main pattern of SSC during the spring tidal cycle was similar to that at site NU, except for low SSC magnitude. However, a different pattern was found during the transition tidal period of 20–23 July and the neap tidal cycle of 24–26 July. The water column kept the low SSC during the transition period (Figure 8b). Significant, short-lived high-SSC events occurred during the neap tidal cycle, with peaks up to 1.0-mab height and durations up to a few hours. During those short-lived high-SSC events, the maximum SSC reached ~18 g/L.

A Butterworth filter was used to remove the tidal oscillations from the 2-min-interval sampling of SSC profiles in the near-bed 1-m layer. Then, the vertical gradient of SSC was calculated by using the filtered SSC profiles. The vertical gradients of SSC at sites NU and SU are displayed in Figure 9. We can see that site NU was characterized by a strong SSC gradient, starting from the tidal transient period and rising to a peak during the neap tidal cycle around 25–26 July. The maximum gradient of SSC reached ~40 g/(L*m). The vertical gradient of SSC was relatively smaller during the spring tidal cycle (Figure 9a), with a typical value of 10 g/(L*m). In some isolated patches, the gradient was up to 20 g/(L*m). At site SU, the vertical gradient of SSC was generally weak, with a typical value of 2–4 g/(L*m) over the neap and spring cycles.

The influence of sediment on density can be estimated using the following equation,

$$\rho = \rho_w + \left(1 - \frac{\rho_w}{\rho_s}\right)C, \quad (4)$$

where ρ_w is the water density that is a function of temperature and salinity, ρ_s is sediment density, and C is the SSC in the water column. Using equation (4), we calculated the sediment-induced gradient Richardson

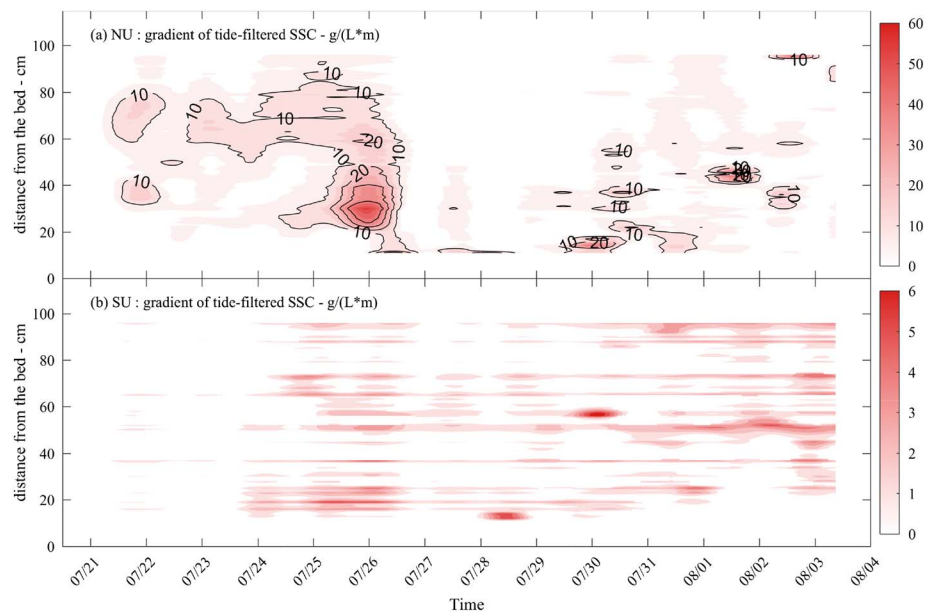


Figure 9. Variation of gradients of tide-filtered suspended-sediment concentration (SSC) in the near-bed 1-m range at sites (a) NU and (b) SU.

number in the lower 1-m column, and the results are plotted in Figure 10. Note that the ASM-derived SSC in each profile did not fully follow the hydrostatic assumption for lower SSC in the upper cell and higher SSC in the lower cell. Due to turbulent mixing, diffusive process, and sediment settling, the SSC at neighboring optical sensors could have strong stochastic patterns, which could lead to a negative value of Ri . In this situation, it is invalid to calculate $\log_{10}(Ri/0.25)$. For the case with higher SSC or within the benthic layer of CBS, the optical sensor of ASM could reach its upper limit and resulted in a constant maximum turbidity value at the measurement site. When this happened, Ri was incomputable in the uniform SSC vertical cells, such as the near-bed 0.2–0.4 mab around 25 July at site NU. These turbulence and sensor upper limit together caused invalid cells, which are shown in Figure 10.

In spite of these blanked cells, the major pattern of the sediment-induced stratification was captured. The occurrence of CBS matched well with a large value of Ri , showing that in such a thin benthic layer, sediment

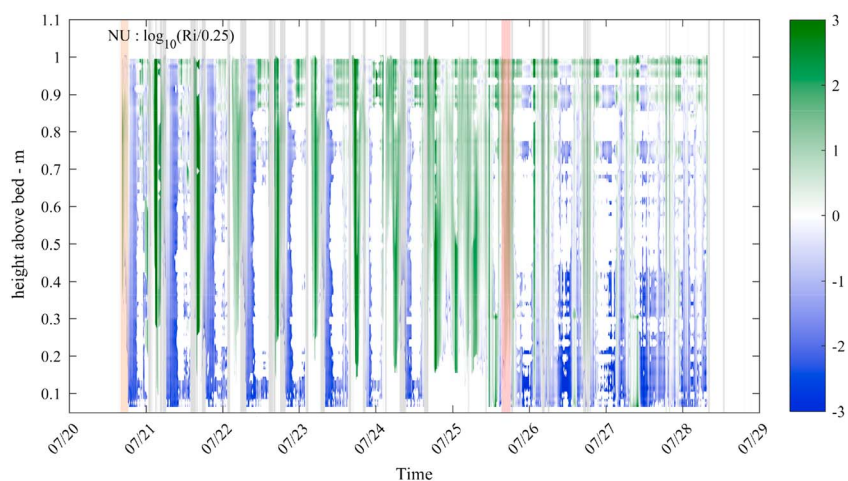


Figure 10. Variation of sediment-density-induced gradient Richardson number with log-scaled contour in the near-bed 1-m range at site NU. The pink shading demonstrates the longest occurrence of concentrated benthic suspension (CBS) at these two tripod sites. The yellow shading indicates the occurrence of CBS longer than 2 hr, and the gray shading shows the occurrence of CBS shorter than 2 hr.

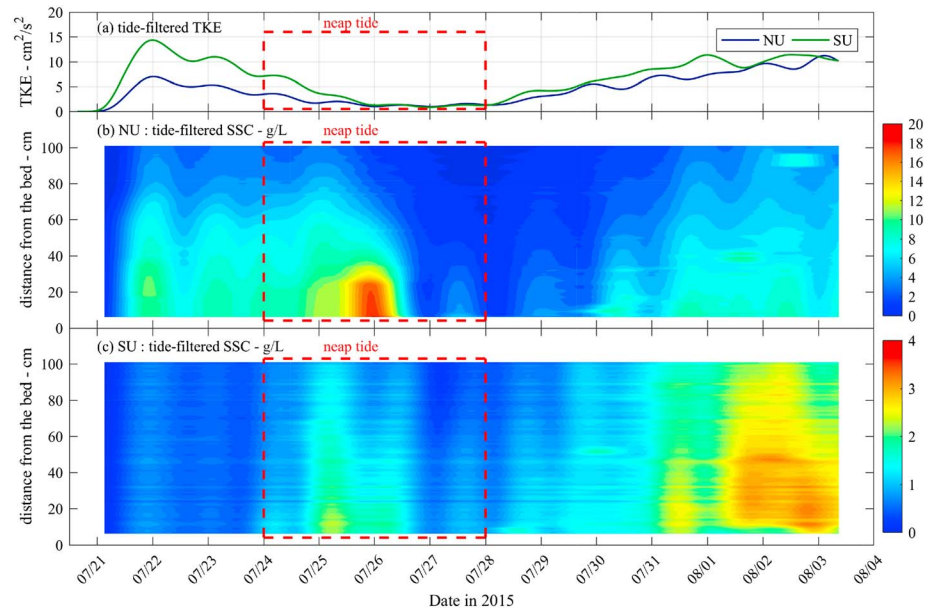


Figure 11. (a) Time series of tide-removed turbulent kinetic energy (TKE) and suspended-sediment concentration (SSC) profiles in the near-bed 1-m range at sites (b) NU and (c) SU. The red dashed boxes indicate the neap tide period.

stratification could be much stronger than the salinity-induced stratification. As a result, it could significantly limit the upward transport of sediment due to the suppression of turbulence.

The mean status of the benthic CBS at sites NU and SU were evaluated using the time series of filtered SSC profiles (Figure 11). We can see that both sites were characterized by highly concentrated mud suspension during the neap tidal cycle. During this period, the two sites were controlled by the same physics, including weak tidal mixing, strong salinity- and sediment-induced stratification, and density-gradient-induced turbulence suppression. All these physical processes favored the formation of CBS. We also estimated the thickness of CBS (Figure 11), which showed a value of $\sim 0.2\text{--}0.3$ m at site NU. At this site, the tide-removed SSC had a maximum value of ~ 20 g/L during the neap tidal cycle, which was much larger than that during the spring tidal cycle. At site SU, the SSC was relatively higher during the neap tidal cycle compared with that during neap-spring transition and tended to be vertically homogenized. This was induced by relatively strong TKE (Figure 3), which produced relatively strong vertical mixing. The filtered SSC vertical gradient demonstrated the TKE's influences on the vertical distribution of CBS. Weak TKE produced a thin, strongly stratified, highly concentrated CBS. Comparatively, relatively strong TKE provided higher mixing energy at site SU, leading to a thick, weakly stratified, lowly concentrated CBS in the lower benthic layer.

5. 1DV CBS Model Simulation

5.1. 1DV Model

To examine the physical processes controlling the formation and breakdown of CBS under the conditions of stratification and suppression of TKE production, we configured a 1DV numerical model based on the FVCOM. FVCOM is an unstructured-grid, three-dimensional (3D), primitive equation ocean numerical model (Chen et al., 2003; Chen, Beardsley, & Cowles, 2006; Chen, Cowles, & Beardsley, 2006; Huang et al., 2008). It uses a nonoverlapped triangular mesh in the horizontal and a terrain-following coordinate in the vertical. The updated version 4.0 of FVCOM has incorporated the full dynamics of sediment transport as a kernel module, which includes both noncohesive and cohesive sediments and their mixtures' interaction.

To simplify the physics of CBS formation, the CBS was considered as a thickness-varying layer with constant sediment concentration, similar to the approach used to calculate fluid mud by Wang and Winterwerp (1992). In general, the concentration of CBS is in the range from ~ 10 to ~ 100 g/L (Winterwerp, 1999). For our measurements, the typical concentration of CBS was about 20 g/L, with a maximum concentration of

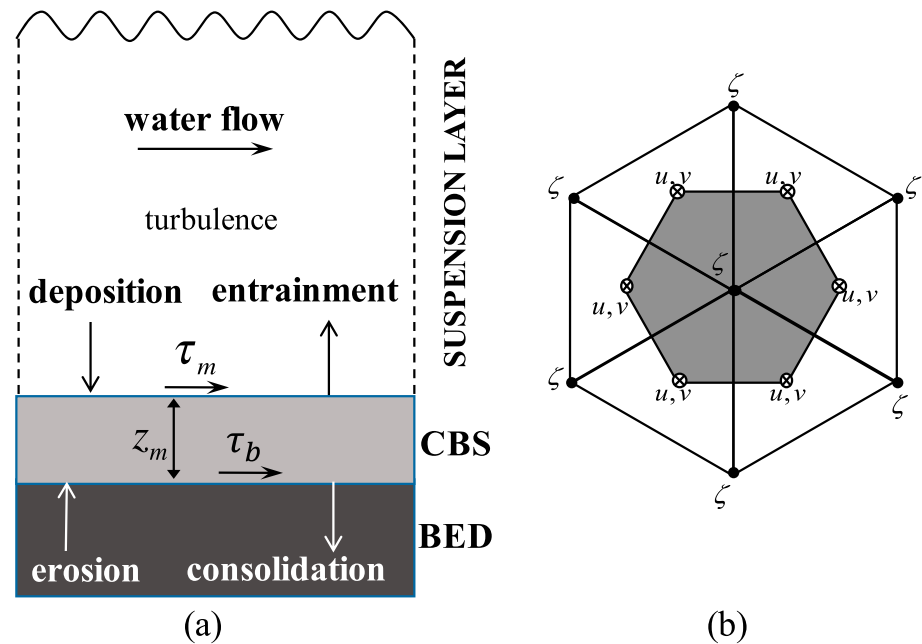


Figure 12. (a) Sketch showing the physical processes considered in the three-layer suspension- concentrated benthic suspension (CBS)-bed system. (b) The model grid with one control volume for momentum in the one-dimensional vertical experiment.

~47.54 g/L, so the fluid-mud dynamics should be applicable. Built on the fluid-mud dynamics, we divided the vertical column from the sea surface to the consolidated seabed into three layers: (1) the suspension layer from the sea surface to the water-CBS interface (where the regular water-sediment mechanism dominated), (2) the CBS layer in the thin benthic layer with a constant, high sediment concentration, and (3) the consolidated bed (Figure 12a). The CBS with the sediment concentration of ~10 g/L exhibited a transition from Newtonian to non-Newtonian behavior (Winterwerp, 1999). The CBS, with the concentration <20 g/L, mainly shows Newtonian flow characteristics, interacting with the ambient flow, and exhibits a similar viscosity to water. When the water-sediment mixture becomes denser with typical concentration range of 20–100 g/L, the CBS layer has been classified as mobile suspension with non-Newtonian behavior, which is moving freely under upper tide-induced shear or bathymetry downslope under the gravity (Manning et al., 2010). Under non-Newtonian condition, an interface that separates the suspension/CBS is referred to as a lutocline. The CBS layer could be stationary or flowing, depending on the laminar shear stress upon the interface between the suspension and CBS layers. In order to simulate the physical process with spring-neap variation, we included the temporal variation of horizontal velocity, but no horizontal transport was defined. The 1DV model was configured with six cells, with all scalar variables at nodes and velocity at cell centers being the same. This treatment enabled us to establish a 1DV model using the 3D code and grid configuration.

As the CBS was treated as a constant-concentration layer, the formation of CBS can be determined by the source and sink of sediment in and out of the CBS. At the interface between suspension and CBS layers, deposition brought sediment into the CBS layer from the upper column, and the entrainment process made the CBS resuspended into the upper suspension layer. At the CBS-bed interface, the seabed could be eroded into a CBS layer when the adequate shear stress was larger than the critical shear stress for erosion, and CBS could also contribute to the seabed through the consolidation (dewatering) process (Figure 12a). The growth/diminishing of CBS could be determined by the sum of deposition, entrainment, erosion, and consolidation processes. It required that the 1DV model resolve the multilayer vertical discretization in the suspension layer to include density stratification, turbulence suppression, and advection. It also needed a depth-averaged CBS layer and finite or infinite thickness of the seabed, depending on the model configuration.

According to the governing equation of the 3D, suspended-sediment transport, the sediment content and local change at a given location and time can be determined by the following equation:

$$\frac{\partial C}{\partial t} + \nabla \cdot (uC) + \frac{\partial(\omega - \omega_s)C}{\partial z} = \frac{\partial}{\partial z} \left(K_M \frac{\partial C}{\partial z} \right), \quad (5)$$

where ∇ represents horizontal derivative; C (g/L) is the SSC; u (m/s) is the horizontal water velocity vector; ω (m/s) and ω_s (m/s) are the vertical water and sediment-settling velocities, respectively; and K_M (m²/s) is vertical eddy viscosity. In this 1DV experiment, $\nabla \cdot (uC)$ was set to zero based on the assumptions of no horizontal gradients for velocities and sediment concentration, which yields

$$\frac{\partial C}{\partial t} + \frac{\partial(\omega - \omega_s)C}{\partial z} = \frac{\partial}{\partial z} \left(K_M \frac{\partial C}{\partial z} \right). \quad (6)$$

The control equations of CBS dynamics, including the continuity and momentum equations, are described as in Wang and Winterwerp (1992):

$$\frac{\partial d_m}{\partial t} + \frac{\partial u_m d_m}{\partial x} + \frac{\partial v_m d_m}{\partial y} = \frac{1}{c_m} \frac{dm}{dt}, \quad (7)$$

$$\frac{\partial u_m}{\partial t} + u_m \frac{\partial u_m}{\partial x} + v_m \frac{\partial u_m}{\partial y} + g \frac{\rho_m - \rho}{\rho_m} \frac{\partial \eta_m}{\partial x} - \Omega v_m + \frac{1}{\rho_m d_m} (\tau_{bx} - \tau_{sx}) = -\frac{1}{\rho_m} \rho g \frac{\partial \eta}{\partial x}, \quad (8)$$

$$\frac{\partial v_m}{\partial t} + u_m \frac{\partial v_m}{\partial x} + v_m \frac{\partial v_m}{\partial y} + g \frac{\rho_m - \rho}{\rho_m} \frac{\partial \eta_m}{\partial y} - \Omega u_m + \frac{1}{\rho_m d_m} (\tau_{by} - \tau_{sy}) = -\frac{1}{\rho_m} \rho g \frac{\partial \eta}{\partial y}, \quad (9)$$

where t is time, d_m is the thickness of CBS layer; u_m and v_m are the eastward and northward components of the CBS's horizontal velocity, respectively; c_m is the sediment concentration within CBS, which is constant in both height and time; ρ_m is the bulk density of CBS; ρ is the density of suspension in the upper layer; Ω is the Coriolis force acceleration coefficient; τ_{bx} and τ_{by} are the shear stresses at the x - and y -directions, respectively, upon the CBS-bed interface; τ_{sx} and τ_{sy} are the shear stresses at the x - and y -directions, respectively, upon the suspension-CBS interface; η_m is the elevation of CBS; and η is the surface elevation of the suspension layer.

Based on the governing equations of CBS dynamics in equations (7)–(9), the formation and evolution of the CBS is not only determined by the source/sink term in equation (7) but also influenced by advection, shear stress at two interfaces, and the Coriolis force. Particularly, this system contains two types of barotropic pressure gradient force. One is due to the elevation gradient of the CBS layer, which is determined by $g \frac{\rho_m - \rho}{\rho_m} \frac{\partial \eta_m}{\partial x}$ and $g \frac{\rho_m - \rho}{\rho_m} \frac{\partial \eta_m}{\partial y}$ for x - and y -components in equations (8) and (9). The other is barotropic pressure gradient force from the upper surface water elevation, defined as $-\frac{1}{\rho_m} \rho g \frac{\partial \eta}{\partial x}$ and $-\frac{1}{\rho_m} \rho g \frac{\partial \eta}{\partial y}$ for x - and y -components in equations (8) and (9).

Under the nongradient assumption of the 1DV model, $\frac{\partial u_m d_m}{\partial x}$, $\frac{\partial v_m d_m}{\partial y}$, $\frac{\partial u_m}{\partial x}$, $\frac{\partial v_m}{\partial y}$, $\frac{\partial \eta_m}{\partial x}$, $\frac{\partial \eta_m}{\partial y}$, $\frac{\partial \eta}{\partial x}$, and $\frac{\partial \eta}{\partial y}$ are all zero. Then, equations (8) and (9) are simplified to

$$\frac{\partial u_m}{\partial t} = \Omega v_m - \frac{1}{\rho_m d_m} (\tau_{bx} - \tau_{sx}), \quad (10)$$

$$\frac{\partial v_m}{\partial t} = \Omega u_m - \frac{1}{\rho_m d_m} (\tau_{by} - \tau_{sy}). \quad (11)$$

The shear stresses at the interface between suspension and CBS layers are calculated by using

$$\begin{pmatrix} \tau_{sx} \\ \tau_{sy} \end{pmatrix} = \begin{pmatrix} \Delta u \\ \Delta v \end{pmatrix} \frac{f_s \rho \sqrt{\Delta u^2 + \Delta v^2}}{8}, \quad (12)$$

and the shear stresses at the interface between CBS and consolidated seabed are calculated by using

$$\begin{pmatrix} \tau_{bx} \\ \tau_{by} \end{pmatrix} = \begin{pmatrix} u_m \\ v_m \end{pmatrix} \frac{\tau_m}{\sqrt{u_m^2 + v_m^2}}, \quad (13)$$

$$\tau_m = \tau_B + \frac{f_m \rho_m}{8} (u_m^2 + v_m^2), \quad (14)$$

where f_s is the friction coefficient between the CBS layer and the upper suspension layer; f_m is the friction coefficient between the CBS layer and the seabed; τ_B is the Bingham yield strength for the transitional behavior from the Newtonian to non-Newtonian CBS, which is set to 0.2 N/m²; u and v are the x - and y -components of the horizontal velocity in the suspension layer, respectively; Δu and Δv are the velocity differences between the upper suspension layer and the CBS layer, respectively, and are given by

$$\Delta u = u - u_m, \quad (15)$$

$$\Delta v = v - v_m. \quad (16)$$

The flow of the CBS was driven by the shear stress (τ_s) between the suspension layer and the CBS layer and by the shear stress (τ_b) between the CBS layer and the seabed. These shear stresses, however, were not determined by the barotropic gradient of the CBS flow or the benthic tidal flow. It was calculated by equations (12) and (13), which only involves local motion. In the 1DV model, the flow of fluid mud under the gradient of CBS's surface was not included. The flow of CBS was purely determined by the local motions of the suspension layer and the CBS layer. If the CBS model is extended to 2D or 3D, the surface gradient of CBS needs to be taken into account.

The total source and sink terms for the CBS formation are calculated by using

$$\frac{dm}{dt} = \text{Settling} - \text{Entrainment} + \text{Erosion} - \text{Dewatering}, \quad (17)$$

in which *Settling* and *Erosion* are the source terms to the CBS formation and *Entrainment* and *Dewatering* are the sink terms. These terms are determined as follows:

$$\text{Settling} = H\left(\frac{\tau_{dm} - \tau_s}{\tau_{dm}}\right) \omega_s C_b \left(\frac{\tau_{dm} - \tau_s}{\tau_{dm}}\right), \quad (18)$$

$$\text{Entrainment} = \frac{2C_s \left(|u_{*,m}|^2 - \frac{\tau_b}{\rho_m} \right) (\vec{u} - \vec{u}_m) + C_\sigma \left(|u_{*,s}|^2 - \frac{\tau_b}{\rho_m} \right) |u_{*,s}|}{\frac{gh\Delta v}{\rho} + C_s (\vec{u} - \vec{u}_m)^2} C_m, \quad (19)$$

$$\text{Erosion} = H\left(\frac{\tau_b - \tau_e}{\tau_e}\right) M_e \left(\frac{\tau_b - \tau_e}{\tau_e}\right), \quad (20)$$

$$\text{Dewatering} = V_0 C_m, \quad (21)$$

where $H()$ is the Heaviside function. The term in the brackets is valid only if its value is positive. C_b is the SSC in the bottom layer of the suspension column attached upon the CBS. τ_{dm} is the critical shear stress for settling, and $\tau_{dm} = 0.1$ N/m². $\tau_b = \sqrt{\tau_{bx}^2 + \tau_{by}^2}$ is the shear stress between the CBS and the consolidated bed, $V_0 = 2.0 \times 10^{-7}$ m/s is the consolidation rate, C_m is the sediment concentration in the CBS layer, and $M_e = 0.001$ kg/(m²·s) is the bulk erosion coefficient. τ_e is the critical shear stress for erosion of the consolidated bed, which is set to 0.2 N/m². $u_{*,s} = \sqrt[3]{u_*^3 + u_{*,m}^3}$, where u_* is the friction velocity of the flow in the suspension layer and $u_{*,m} = f_s(u - u_m)^2$. The empirical coefficients are $C_s = 0.25$ and $C_\sigma = 0.42$. The other parameters in the simulation were configured as follows: $c_m = 75.0$ g/L, $f_s = 0.032$, $f_m = 0.05$, and $\omega_s = 0.006$ m/s.

The tidal forcing for the 1DV model was specified by the multiple astronomical tidal constituents, which were calculated using the harmonic analysis at site NU. The T_tide MATLAB package developed by Pawlowicz et al. (2002) was used for tidal harmonic analysis for 15-day time series velocities at site NU. In our 1DV model, the tidal flow was generalized by specifying the periodically changing pressure gradient. This gradient forcing generated the barotropic tidal current throughout the water column. With the inclusion of vertical eddy viscosity and bottom friction under a stratified condition, the tidal velocity varied with depth and the vertical

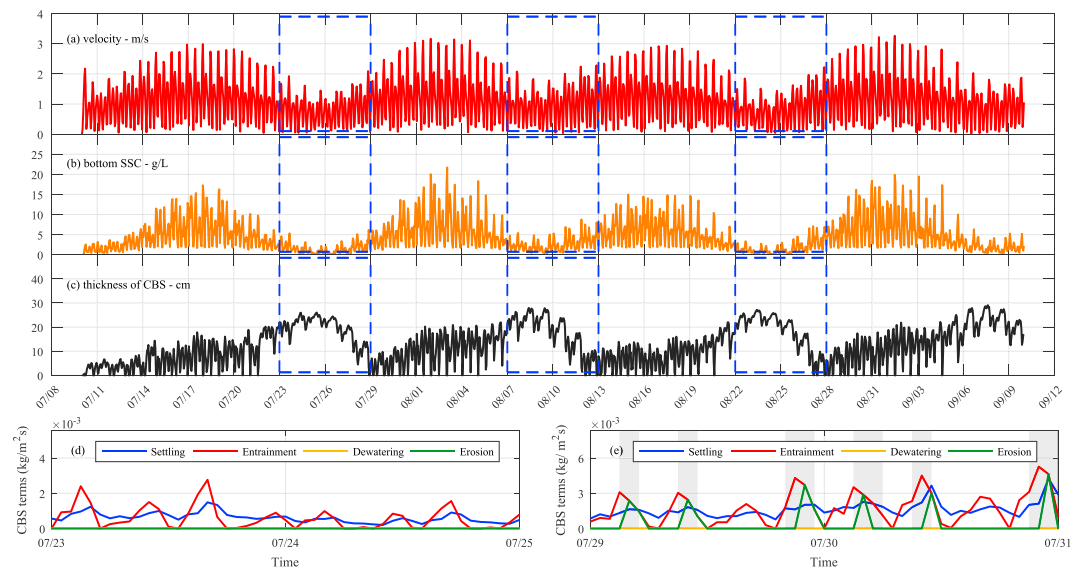


Figure 13. Time series of (a) tide velocity; (b) near-bottom suspended-sediment concentration (SSC) in the suspension layer; and (c) thickness of concentrated benthic suspension (CBS); and the contributions of settling, entrainment, dewatering, and erosion (d) in the stable CBS period from 23 to 25 July and (e) in the oscillated CBS period from 29 to 31 July. The dashed blue box indicates the neap tidal period, and the shaded areas in the right panel are the periods without the CBS in the benthic layer.

shear of currents against vertical stratification generates tidal mixing in the vertical. In addition to tidal-induced turbulent mixing, the tide flow also created the benthic flow upon the CBS. Both tidal-induced mixing and benthic flow directly affects the growth and subduction of the CBS.

The grid configuration for the 1DV model is shown in Figure 12b, which contains seven triangular nodes for scalar variables and six cells for vector variables. These nodes and cells comprised one controlling volume for FVCOM numerical space discretization (Chen et al., 2003, 2013). To satisfy the nongradient assumption in the horizontal, all triangular cells were set to a uniform depth of 11 m as shown at site NU. The vertical column was discretized into 50 uniform layers. The vertical eddy viscosity (K_m) and thermal diffusion coefficients (K_h) were parameterized using the Mellor and Yamada (1982) level 2.5 (MY-2.5) turbulent closure model. The density effect, including sediment and salinity, was considered in equation (4) and taken into account when K_m and K_h were calculated. The suppression of turbulence under stratification and density were also included in the model by using equation (3).

5.2. Modeling Results

The simulation, marked as Exp CBS, was run with initial conditions of zero velocity, zero SSC in the water column, and zero thickness of CBS. The model simulation was conducted with the inclusion of tidal oscillation at site NU for the period from 10 July to 10 September 2015. The period covered four neap-to-spring cycles, with a spring maximum velocity of ~ 3.0 m/s and a neap maximum velocity of ~ 1.0 m/s (Figure 13a); the model was able to reconstruct the observed tidal velocity and mixing as site NU.

Exp CBS reproduced a typical spring-to-neap pattern of the sediment concentration in the bottom suspension layer, a layer that was close to and directly covered the CBS layer. In this layer, the SSC was high at the maximum spring ebb and flood as the tidal velocity was the strongest, and the SSC was low during the neap tidal cycle as the tidal velocity was weak (Figure 13b). The SSC peaks during the spring tidal cycle ranged from 10 to 20 g/L, depending on the magnitude of the tidal velocity. The SSC was about 1–3 g/L at the lower bottom during the neap tidal cycle. This model-simulated spring-neap pattern was in agreement with the observed SSC variation in the suspension layer.

The periods for two typical cases with and without stable CBS in the benthic layer were selected to check the contributions of CBS terms in equations (18)–(21) (Figures 13d and 13e). During the weak mixing neap tide,

the near-bed shear stress was less than the critical shear stress for erosion τ_e , leading to a zero contribution of the erosion term in the formation of the CBS (Figure 13d). The dewatering (consolidating) contribution was constant when the CBS was included, although it was weak with a magnitude of $0.036 \text{ kg}\cdot\text{m}\cdot\text{s}^{-1}$. Therefore, the variation of the CBS thickness was mainly determined by the terms of settling and entrainment, revealing a relatively stable settling effect.

The entrainment effect changed with the tide flow. When the tide flow became large, the CBS was unstable due to stronger tidal mixing. When the CBS was present, the contributions of the four terms showed similar patterns as those found during the stable CBS period. However, in the case without CBS (shaded regions in Figure 13e), the consolidation was invalid. The erosion term became significant. The entrainment was practically the eroded amount into the upper column. Therefore, the formation of the CBS was determined by the residual due to erosion and settling. When settling overwhelmed erosion, the CBS was formed in the benthic layer.

During the spring tidal cycle, the CBS was found in its formation process with large variation, suggesting that the CBS was dynamically unstable over a short period during the spring tidal cycle. In this period, the formation of CBS was mainly caused by the significant sediment deposition from the suspension layer under a weak current condition. In this case, the sediment was easily brought to the suspension layer through strong tide-induced entrainment. The 1DV model did reproduce the stable CBS during the neap tide and the high-frequency formation and breakdown of CBS during the spring tide (Figure 13a). These results matched well with the observed CBS occurrences at site NU at the same tidal period, as shown in Figure 4.

During the neap tidal cycle, the sediment settling under a weak tidal condition was confined in the bottom layer, which caused the sediment gradually deposited into the CBS. With the weak tidal mixing, the current was unable to provide adequate TKE production, so the tidal straining was too weak to promote the entrainment process and to resuspend the CBS from the bottom benthic layer. In this case, the dewatering activity was relatively slow, which consolidated the CBS into the seabed. These processes jointly resulted in the stable formation of CBS, which was characterized with a thickness of $\sim 20 \text{ cm}$.

5.3. SSC in the Suspension Layer

To identify and qualify the contributions of different physical processes on the variability of suspension layer, we ran Exp no-CBS, which has the same configuration as Exp CBS, except without the inclusion of CBS dynamics. In Exp no-CBS, we only considered the regular sediment processes of deposition and erosion with one suspension-bed interface in the system. In Exp CBS, the deposited sediment first settled into the CBS when it was already formed or initialized the CBS above the bed. In Exp no-CBS, the sediment directly sank into the seabed. By comparing the two experiments (Figure 14), we can examine different outcomes of the deposited sediment from the suspension layer to the CBS layer, or to the consolidate bed.

When a stable CBS layer was formed, such as during the neap tide cycle, the top of the CBS layer was practically the lutocline. The vertically averaged SSC in Exp CBS was lower than that in Exp no-CBS (Figure 14a). This pattern remained true even at the bottom of the suspension layer (Figure 14b). It indicates that the lutocline did prevent upward mixing during the neap cycle.

During the spring cycle, the lutocline was not stable due to stronger mixing. The entrainment in Exp CBS was significant, and the sediment in the water column returned to the bed through consolidation, which was a slow process. Comparatively, in Exp no-CBS the sediment was returned from water column to seabed by settling process, which was a quick process. And bed sediment needed stronger bottom shear stress, larger than τ_e , to resuspend by erosion process. It indicates that the water column in Exp CBS could contain more sediment in the spring tide. Therefore, the difference of numerically dealing with the source/sink term at the seabed in these experiments led to higher sediment concentration in the water column in Exp CBS during the spring tide (Figure 14).

These 1DV model results support the observations from our tripods and anchored vessels and confirm the importance of benthic sediment dynamics. The weak tidal mixing and density-induced stratification can produce stable CBS during the neap tidal cycle and short-lived CBS during the spring tidal cycle. This 1DV model was included in the official release of FVCOM version 4.0 as an independent module, which can be downloaded from the FVCOM website (<http://fvcom.smast.umassd.edu/fvcom/>).

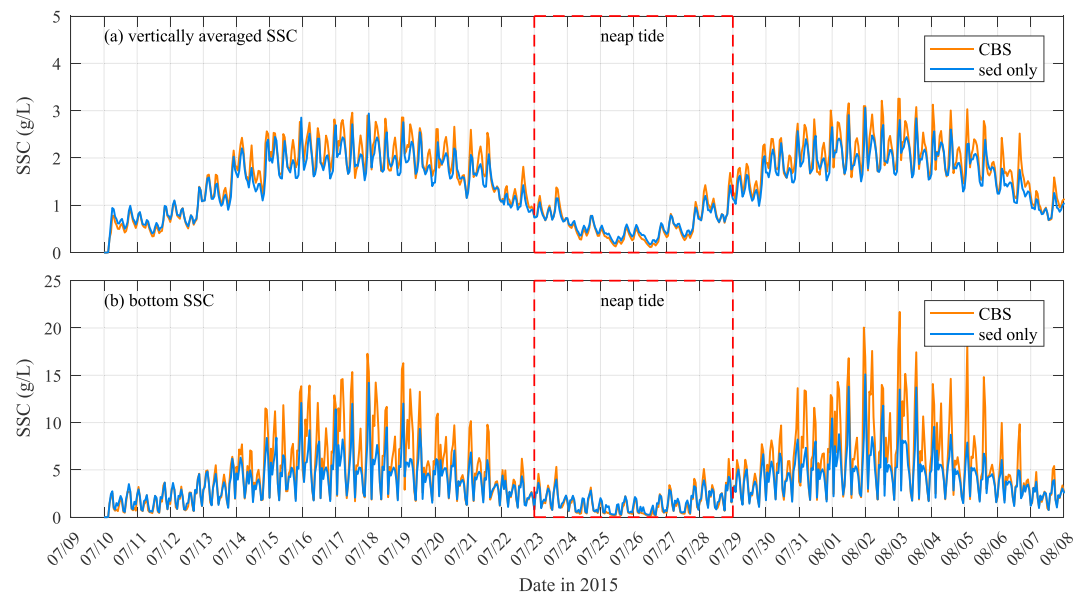


Figure 14. Time series of near-bottom suspended-sediment concentration (SSC) in the suspension layer with (yellow) and without (blue) considering the dynamics of concentrated benthic suspension (CBS). The red dashed box indicates the neap tide period.

6. Discussion

6.1. Hindered Settling

The settling velocity has a great influence on the effectiveness and speed of the deposition. Under the high-concentration CBS, the sediment particles hindered each other during settling, and the effective settling velocity was reduced as a result. Under an environment with the sediment concentration from a few to ~ 100 g/L, the hindered settling could significantly decrease the effective settling velocity with various gelling concentrations from 40 to 120 g/L (Winterwerp & Van Kesteren, 2004). This process also contributed to the formation and sustaining of CBS. The typical settling velocity of cohesive mud in the turbidity maximum zone of the Changjiang Estuary was about 0.6 mm/s (Shao et al., 2011). If the gelling concentration is about 40 g/L (Ross, 1988), the sediment concentration of 20 g/L can reduce the settling velocity to less than 0.1 mm/s. It can help the sediment stay in the fluid much longer until it touches the seabed. Larger gelling concentrations, such as 80 and 120 g/L, can also yield a significant reduction of settling velocity.

6.2. Formation and Breakdown of CBS

Both the observations and 1DV numerical model results suggested that the formation of CBS was controlled by the complex hydrodynamic and sediment processes. The 1DV model revealed that the deposition from upper suspension column and entrainment of sediment determines the height of the CBS during the formation and breakdown of the CBS. The tidal mixing determines the stability of the CBS, which is verified by observation and modeling results, TKE production and suppression, and density-induced stratification from salinity, and sediment also had significant contribution on the CBS formation.

Taking a typical CBS event at site SU at 03:00 on 24 July 2015 as an example, with the occurrence of CBS during the period from the late flood to early ebb tide (Figure 15), the mixing efficiency played a critical role in the formation and breakdown processes of the CBS. When the mixing efficiency decreased during the late flood tide, especially when the two-layer flow was established (Figures 15b and 15c), the benthic TKE decreased and the sediment significantly accumulated in the benthic layer (Figure 15d), and the CBS was formed and sustained even after the mixing efficiency reached the minimum.

The salinity-induced stratification has been taken into account for the estimate of mixing efficiency in equation (1). The vertical salinity gradient also reached its maximum from the late flood to early ebb tide

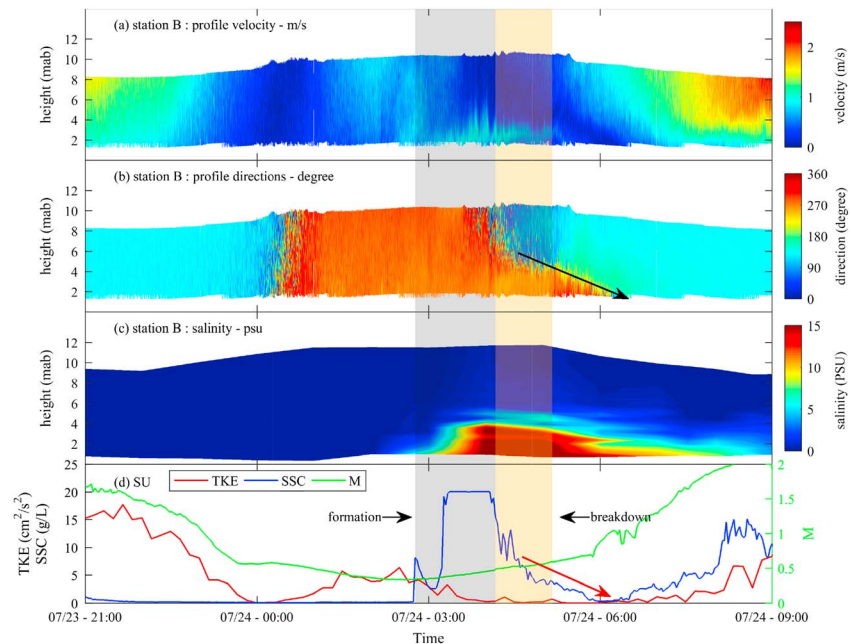


Figure 15. Vertical distributions of (a) tidal flow, (b) direction, and (c) salinity, and (d) time series of benthic turbulent kinetic energy (TKE), suspended-sediment concentration (SSC), and mixing efficiency during the formation and breakdown of a selected concentrated benthic suspension event at site SU on 03:00 on 24 July 2015. Gray- and yellow-shaded regions indicate the formation stage and breakdown stage of the CBS, respectively.

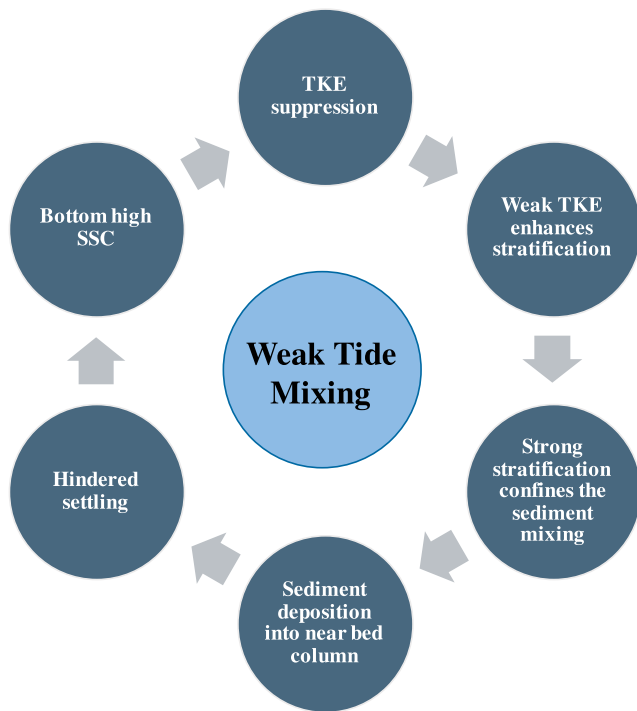


Figure 16. The positive feedback loop of physical processes controlling the formation process of concentrated benthic suspension during weak tidal mixing. TKE = turbulent kinetic energy; SSC = suspended-sediment concentration.

(Figure 15c). It favored the reduction of mixing efficiency. With the suppression of sediment- and salinity-induced density, the benthic TKE kept its minimum during the stratification.

The weak tidal mixing was the background hydrodynamic condition for sediment deposition, in which the settling velocity was significantly reduced through hindered effects. The freshwater discharge from the upstream of the river and saltwater intrusion from the inner shelf formed a two-layer salinity structure in the vertical, which enhanced stratification. The stratification greatly limited vertical mixing and confined the sediment in the lower water column. The accumulated sediment produced a strong SSC gradient in the near-bed layer, which reduced sediment diffusivity and TKE production. This process reduced vertical mixing and sediment diffusion and enhanced sediment-induced stratification. These physical processes functioned as parts of a positive feedback loop (Figure 16) and increased the formation of CBS until stronger tidal mixing occurred.

The mud accumulation through deposition process from the suspension layer was the major source of sediment to create and sustain the CBS. During the spring tidal cycle, the sediment from the CBS through entrainment or from the seabed through erosion increased the suspended load in the water column, which, subsequently, deposited under a weak tide condition during the neap tidal cycle. The deposition mainly occurred during the weak-current tidal phase, in both spring and neap tidal cycles. Based on the tripod observations, we noticed that the deposition took place during the transition from late flood to early ebb and from late ebb to early flood. However, not all depositions from these two periods could form CBS, even during the neap tidal cycle. Statistically speaking, CBS was only detected during the late-flood to early-ebb period. Therefore, the

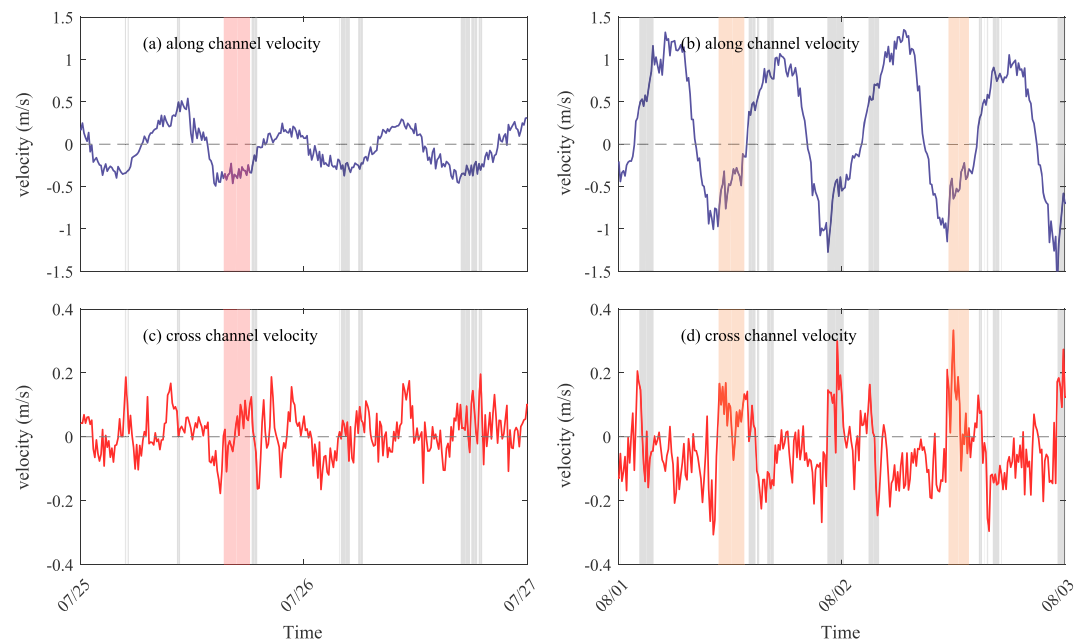


Figure 17. The (top) along-channel and (bottom) cross-channel velocities during (left) neap and (right) spring cycles at site NU. Positive values in along-channel velocity indicate flood current, and positive values in cross-channel velocity indicate northward flow crossing the channel. The pink shading marks the longest occurrence of concentrated benthic suspension (CBS) at site NU. The yellow shading indicates the occurrence of CBS longer than 2 hr, and the gray shading shows the occurrence of CBS shorter than 2 hr.

formation of CBS was related not only to the sediment source provided by deposition but also to the inherent hydrodynamics.

The breakdown of CBS was also highly correlated to the combined mixing efficiency. The breakdown mainly occurred during the early-ebb period; when the ebb tide current increased (Figures 15a and 15b), the tide-induced mixing efficiency started to increase in the water column (Figure 15d). Hence, the entrainment from CBS to the upper suspension layer was increased. With the developing of the ebb tide, the salinity gradient was weakened, so was the salinity-induced stratification (Figure 7). It was mainly an opposite procedure of the physical feedback loop in Figure 15.

Although the increased tidal mixing could enhance entrainment and then trigger the breakdown process, the contributions of horizontal advection and transport need our attention, too. After the CBS was formed, the benthic current was still in the flood-current direction, pushing the CBS in the upstream direction (arrow in Figure 15b); it matched with the breakdown of the CBS, and the SSC reached its minimum when the benthic current reached its tipping point from flood to ebb direction (arrow in Figure 15d). Therefore, the breakdown of CBS was associated with joint effects of increased vertical mixing and horizontal advection.

6.3. Possible Source and Movement of CBS

During the analysis of tripod measurements and numerical simulations, the CBS formation and breakdown were treated as 1DV processes. However, besides the vertical physical processes, horizontal advection and transport are also important contributors to the sediment variation at sites SU and NU.

Taking site NU as an example, the flow was flood dominant during both neap and spring cycles (Figures 17a and 17b). But the along-channel flow decreased significantly from 0.5 to ~0.1 m/s after the CBS was formed in Exp CBS. The lateral cross-channel flow also had a contribution to the CBS's movement, which mostly flowed northward. It had the same order of magnitude (0.1–0.2 m/s) as the along-channel current.

The horizontal current can result in large-scale distribution of CBS. Based on the average horizontal velocity (~0.3 m/s in the along-channel direction and ~0.1 m/s in the cross-channel direction) and the maximum sustaining duration of CBS (2.83 hr at site NU), the CBS could cover an area of 3 km × 1 km approximately.

Besides the local production of CBS, the remote source of CBS could be an additional source of sediment. With the current speed and direction during the CBS and the estimate of the range, the sediment of the CBS at site NU could come from its southeastern region, near or close to the main channel. Previous field observations had revealed the existence of benthic fluid mud within the main channel (Liu et al., 2011; Song et al., 2013). This could be a potential sediment source, from which sediment was transported to the region around site NU under the advection effects shown in Figure 17, forming the CBS.

The advection of suspended sediment might have contributed to the formation and breakdown of the CBS. However, identification of the effect of advection requires higher-resolution observations over a broader area. The numerical model also needs to be extended to 3D and be fully coupled with a hydrodynamic model covering the whole North Passage and its adjacent region, in order to study this effect.

The different behaviors of the CBS between sites NU and SU could also be attributed to the hydrodynamic condition and its induced advection and movement of suspended sediment. Sites NU and SU were located on two sides of the main channel of the North Passage. Although the two tripod sites were geographically close to each other, they had significant differences of physics and sediment dynamics. The benthic saltwater intrusion that occurred in flood tide mainly flowed at the north side of the main channel (Figure 17 in Ge et al., 2013), which produced stronger stratification condition at the north side. Comparatively, the saltwater intrusion and the vertical gradient of salinity south of site SU was weaker (Figure 3e). It led to stronger mixing efficiency at site SU, which potentially carried more bottom sediment into the upper water column. Therefore, site SU had lower-frequency occurrence and lower concentration of CBS formation (Figure 3f).

6.4. Perspectives on General Physics

Geyer and MacCready (2014) classified estuaries based on mixing number M and freshwater Froude number Fr_f . Fr_f is defined as

$$Fr_f = U_R / (\beta g S_{\text{ocean}} H)^{1/2} \quad (22)$$

where U_R is the net velocity due to river flow scaled by the maximum possible frontal propagation speed. Defining the estuarine Fr_f - M space, the stratification level of individual estuary could be estimated. This Fr_f - M space has a broader range, which covers not only the whole estuary due to large oscillation of freshwater discharge in different seasons but also tide current and stratification level in different periods. The CBS formation, however, is a feature driven by local physical and sediment dynamics. The stratification and mixing conditions during the CBS formation at a local site was difficult to be classified based on the originally defined Fr_f - M parameter space. For this reason, a modified parameter method for evaluating mixing efficiency is proposed in section 4.1 through a moving-average algorithm with an average period of a $T/2$ tidal cycle. The method is aimed to provide an estimation of mixing efficiency for local measurements. In this method, the freshwater Froude number is localized as

$$Fr_{fl} = U_{RL} / (\beta g S_{\text{ocean}} H)^{1/2} \quad (23)$$

where U_{RL} is the local net velocity due to river flow's contribution. The U_{RL} could be estimated by a difference between the total residual flow (U_{res}) and tidal-induced residual flow (U_T) over a tidal cycle, that is,

$$U_{RL} = U_{res} - U_T \quad (24)$$

In our case, at NU site, Fr_{fl} ranges from 0.6 in the neap tidal cycle to 1.7 in the spring tidal cycle. Correspondingly, M varies from 0.1 to 3.5. Low Fr_{fl} means that the local formation and subduction plays a major role in CBS dynamics, while high Fr_{fl} suggests that the horizontal transport may prevail.

Both the near-bed tripod measurement and numerical simulation revealed that in the time-dependent salt wedge system the effect of tidal modulation on the formation of CBS varies with stratification and tide mixing. The moving-average algorithm over a time scale of tidal cycle allows us to quantify time-dependent mixing efficiency under a condition with rapid changes of tidal currents and surface-bottom salinity difference. With this method, the tidal-induced mixing efficiency is quantitatively related with the formation of the CBS. This is useful for CBS studies in a time-dependent stratified estuary, since the

stratification level is not stable, not only during a ~14-day spring-neap cycle but also during a semidiurnal M_2 cycle at individual spring/neap periods.

Our observations revealed that the CBS has higher probability of occurrence with mixing efficiency of 0.1–0.5 in neap cycles and 0.5–2 in spring cycles. It is possible to extend this result to similar tide-mixing/stratification condition when dealing with the CBS or high-concentration suspension under a time-dependent stratified condition. For example, the Pearl River in the South China Sea is a similar time-dependent salt-wedge estuary characterized with the interaction of river discharge-induced buoyancy and tidal-driven flows. In that estuary, the stable vertically stratified condition can lead to a higher near-bottom sediment suspension at the edge of salinity plume near the river mouth during the neap cycle than during the spring cycle, with a maximum SSC of ~2.38 g/L (Gong et al., 2014; Ren & Wu, 2014). Using the data displayed in Ren and Wu (2014), we estimated the M value at the maximum suspension time during the neap cycle, which was ~0.37. This value is in the range that is consistent with what we found in the Changjiang River Estuary. The Magdalena River is located in the tropical region, Colombia, South America. Restrepo et al. (2018) used Fr_f to determine the balance between the river advection and vertical stratification. The resulting bottom SSC is ~10 g/L during the low stream flow period, which is close to a value required for the CBS formation. The Fr_f - M parameter space could be applied to estimate local mixing efficiency for CBS formation.

In addition, the timing of the CBS occurrence observed in this study could serve as an additional general indicator applicable for other similar periodic stratified estuaries with tidal modulation. In those types of estuaries, the CBS could be found under a strong stratification condition over the transition period from late-flood tide to early-ebb tide.

The observed characteristics of the short life and thin layer of CBS in the Changjiang River Estuary raise a challenge for the future numerical simulation. It requires a numerical model capable of not only having a high-resolution discretization on horizontal, vertical, and temporal scales but also being driven with complete physics, including bed-CBS-water interactions and suppression of turbulence by stratification from salt and sediment. Otherwise, the numerical model could either overpredict the height of pycnocline above the seabed or fail to resolve the vertical distribution of baroclinic gradient force. As a result, the vertical SSC gradient could be underestimated.

7. Conclusions

Two tripod systems equipped with multiple state-of-the-art instrument sensors, plus two anchored vessels, were deployed to monitor benthic concentrated suspension in the North Passage of the Changjiang Estuary. The observed data indicated that the formation of CBS (>15 g/L) was a common feature in the turbidity maximum zone in the study region. High-frequency CBS occurrences were found at the two tripod sites from the late-flood to early-ebb tidal period, especially during the neap tidal cycle. The mean thickness of CBS was about 20–30 cm above the seabed, and the CBS had short life of existence, less than 2.8 hr.

The physics involved, including tidal mixing, turbulence, and stratification, were examined, indicating that the weak tidal mixing from late-flood to early-ebb period is a key physical factor in the formation. The sediment- and salinity-induced stratification created a significant two-layer structure in the vertical, which greatly limited vertical mixing and confined the sediment within the benthic layer. The higher density in the benthic layer greatly reduced diffusivity and TKE production. These physical processes worked as a positive feedback loop.

A 1DV process-based CBS model was developed. It successfully revealed the formation and breakdown of CBS under different tidal conditions during spring-neap period. It revealed that the weak tidal mixing during the neap tidal cycle formed a stable CBS as observed at site NU, and higher-frequency formation and breakdown of CBS in the spring tidal cycle. The weak tidal mixing at the late-flood stage during the neap tidal cycle constrained the tidal straining of the boundary layer into the bottom and brought the benthic mud suspension into the upper water column. Our observations showed that the stratified tidal mixing parameter M under a weak mixing condition during the late-flood to early-ebb period was mainly influenced by the stratification caused by the saltwater intrusion. In the other deposition stage during the late-ebb to early-flood period, both sites NU and SU were controlled by the freshwater discharged from the upstream

river, and the water column was less stratified, producing relatively strong tidal mixing compared with that during the late-flood to early-ebb period.

It should be noted that CBS's identification in this paper was carried out through the indirect optical backscattering sensor with calibration against the sediment collected in the field. If direct sampling of CBS is required in future studies, it should be conducted in the late-flood and early-ebb period with stronger vertical salinity gradient, based on the results in this paper. Additionally, high-frequency sampling method (10- to 20-min interval) needs be applied due to CBS's short life cycle.

Acknowledgments

This work is supported by the National Key R&D Program of China (Grant No. 2016YFA0600903), the NSFC project (Grant Nos. 41776104, 41476076, and 51320105005), the MOST project (Grant No. 2016YFE0133700), and the KNAW project (Grant No. PSA-SA-E-02). The development of cohesive sediment modules and 1DV module in FVCOM was supported by Prof. Chen's Montgomery Charter Chair Education Fund at the University of Massachusetts and U.S. NOAA FVCOM technical support grant (No. A101176) from CINAR. The students and crew members who helped conduct the observations are greatly appreciated. All data sets used in this study are publicly available at <https://figshare.com/s/1fbd648cc15d796a10de>. The authors appreciate three anonymous reviewers for their valuable suggestions.

References

- Baldock, T. E., Tomkins, M. R., Nielsen, P., & Hughes, M. G. (2004). Settling velocity of sediments at high concentrations. *Coastal Engineering*, 51(1), 91–100. <https://doi.org/10.1016/j.coastaleng.2003.12.004>
- Bruens, A. (2003). Entraining mud suspensions. (PhD thesis). Delft University of Technology
- Bruens, A., Kranenburg, C., & Winterwerp, J. (2002). Physical modelling of entrainment by a concentrated benthic suspension. *Proceedings in Marine Science*, 5, 109–124.
- Bruens, A. W., Winterwerp, J. C., & Kranenburg, C. (2012). Physical and numerical modeling of the entrainment by a high-concentration mud suspension. *Journal of Hydraulic Engineering*, 138(6), 479–490. [https://doi.org/10.1061/\(ASCE\)HY.1943-7900.0000545](https://doi.org/10.1061/(ASCE)HY.1943-7900.0000545)
- Burchard, H., Hetland, R. D., Schulz, E., & Schuttelaars, H. M. (2011). Drivers of residual estuarine circulation in tidally energetic estuaries: Straight and irrotational channels with parabolic cross section. *Journal of Physical Oceanography*, 41(3), 548–570. <https://doi.org/10.1175/2010JPO4453.1>
- Chen, C., Beardsley, R., Cowles, G., Qi, J., Lai, Z., Gao, G., et al. (2013). An unstructured grid, finite-volume community ocean model FVCOM user manual, SMAST/UMASSD-13-0701, New Bedford, Mass. Retrieved from <http://fvcom.smast.umassd.edu/fvcom/>
- Chen, C., Beardsley, R. C., & Cowles, G. (2006). An unstructured grid, finite-volume coastal ocean model (FVCOM) system, special issue entitled "Advance in Computational Oceanography". *Oceanography*, 19(1), 78–89. <https://doi.org/10.5670/oceanog.2006.92>
- Chen, C., Cowles, G., & Beardsley, R. C. (2006). An unstructured grid, finite-volume coastal ocean model: FVCOM user manual (2nd ed., p. 45) SMAST/UMASSD Technical Report-06-0602.
- Chen, C., Liu, H., & Beardsley, R. C. (2003). An unstructured, finite-volume, three-dimensional, primitive equation ocean model: Application to coastal ocean and estuaries. *Journal of Atmospheric and Oceanic Technology*, 20(1), 159–186. [https://doi.org/10.1175/1520-0426\(2003\)020<0159:AUGFVT>2.0.CO;2](https://doi.org/10.1175/1520-0426(2003)020<0159:AUGFVT>2.0.CO;2)
- Chen, C., Xue, P., Ding, P., Beardsley, R., Xu, Q., Mao, X., et al. (2008). Physical mechanisms for the offshore detachment of the Changjiang Diluted Water in the East China Sea. *Journal of Geophysical Research*, 113, C02002. <https://doi.org/10.1029/2006JC003994>
- Cuthbertson, A., Dong, P., King, S., & Davies, P. (2008). Hindered settling velocity of cohesive/non-cohesive sediment mixtures. *Coastal Engineering*, 55(12), 1197–1208. <https://doi.org/10.1016/j.coastaleng.2008.05.001>
- Dutta, S., Cantero, M. I., & Garcia, M. H. (2014). Effect of self-stratification on sediment diffusivity in channel flows and boundary layers: A study using direct numerical simulations. *Earth Surface Dynamics*, 2(2), 419–431. <https://doi.org/10.5194/esurf-2-419-2014>
- Ge, J., Chen, C., Qi, J., Ding, P., & Beardsley, R. C. (2012). A dike-groyne algorithm in a terrain-following coordinate ocean model (FVCOM): Development, validation and application. *Ocean Modelling*, 47(C), 26–40. <https://doi.org/10.1016/j.ocemod.2012.01.006>
- Ge, J., Ding, P., & Chen, C. (2015). Low-salinity plume detachment under non-uniform summer wind off the Changjiang Estuary. *Estuarine, Coastal and Shelf Science*, 156, 61–70. <https://doi.org/10.1016/j.ecss.2014.10.012>
- Ge, J., Ding, P., Chen, C., Hu, S., Fu, G., & Wu, L. (2013). An integrated East China Sea-Changjiang Estuary model system with aim at resolving multi-scale regional-shelf-estuarine dynamics. *Ocean Dynamics*, 63(8), 881–900. <https://doi.org/10.1007/s10236-013-0631-3>
- Ge, J., Shen, F., Guo, W., Chen, C., & Ding, P. (2015a). Estimation of critical shear stress for erosion in the Changjiang Estuary: A synergy research of observation, GOCI sensing and modeling. *Journal of Geophysical Research: Oceans*, 120, 8439–8465. <https://doi.org/10.1002/2015jc010992>
- Ge, J.-Z., Ding, P.-X., Li, C., Fan, Z.-Y., Shen, F., & Kong, Y.-Z. (2015b). Estimation of sediment transport with an in-situ acoustic retrieval algorithm in the high-turbidity Changjiang estuary, China. *China Ocean Engineering*, 29(6), 903–915. <https://doi.org/10.1007/s13344-015-0063-6>
- Geyer, W. R. (1993). The importance of suppression of turbulence by stratification on the estuarine turbidity maximum. *Estuaries*, 16(1), 113–125. <https://doi.org/10.2307/1352769>
- Geyer, W. R. (2010). Estuarine salinity structure and circulation. In A. Valle-Levinson (Ed.), *Contemporary Issues in Estuarine Physics* (pp. 12–26). Cambridge, UK: Cambridge University Press. <https://doi.org/10.1017/CBO9780511676567.003>
- Geyer, W. R., & MacCready, P. (2014). The estuarine circulation. *Annual Review of Fluid Mechanics*, 46(1), 175–197. <https://doi.org/10.1146/annurev-fluid-010313-141302>
- Geyer, W. R., & Ralston, D. (2011). The dynamics of strongly stratified estuaries. In E. Wolanski & D. McLusky (Eds.), *Treatise on estuarine and coastal science* (Vol. 2, pp. 37–51). London, UK: Academic Press. <https://doi.org/10.1016/B978-0-12-374711-2.00206-0>
- Gong, W., Jia, L., Shen, J., & Liu, J. T. (2014). Sediment transport in response to changes in river discharge and tidal mixing in a funnel-shaped micro-tidal estuary. *Continental Shelf Research*, 76(C), 89–107. <https://doi.org/10.1016/j.csr.2014.01.006>
- Hu, K., Ding, P., Wang, Z., & Yang, S. (2009). A 2D/3D hydrodynamic and sediment transport model for the Yangtze Estuary, China. *Journal of Marine Systems*, 77(1–2), 114–136. <https://doi.org/10.1016/j.jmarsys.2008.11.014>
- Huang, H., Chen, C., Cowles, G. W., Winant, C. D., Beardsley, R. C., Hedstrom, K. S., & Haidvogel, D. B. (2008). FVCOM validation experiments: Comparisons with ROMS for three idealized barotropic test problems. *Journal of Geophysical Research*, 113, C07042. <https://doi.org/10.1029/2007JC004557>
- Jiang, C., Swart, H. E., Li, J., & Liu, G. (2013). Mechanisms of along-channel sediment transport in the North Passage of the Yangtze Estuary and their response to large-scale interventions. *Ocean Dynamics*, 63(2–3), 283–305. <https://doi.org/10.1007/s10236-013-0594-4>
- Kranenburg, C. (1994). The fractal structure of cohesive sediment aggregates. *Estuarine, Coastal and Shelf Science*, 39(6), 451–460. [https://doi.org/10.1016/S0272-7714\(06\)80002-8](https://doi.org/10.1016/S0272-7714(06)80002-8)
- Li, J., & Zhang, C. (1998). Sediment resuspension and implications for turbidity maximum in the Changjiang Estuary. *Marine Geology*, 148(3–4), 117–124. [https://doi.org/10.1016/S0025-3227\(98\)00003-6](https://doi.org/10.1016/S0025-3227(98)00003-6)

- Li, X., Zhu, J., Yuan, R., Qiu, C., & Wu, H. (2016). Sediment trapping in the Changjiang Estuary: Observations in the North Passage over a spring-neap tidal cycle. *Estuarine, Coastal and Shelf Science*, 177(c), 8–19. <https://doi.org/10.1016/j.ecss.2016.05.004>
- Liu, G., Zhu, J., Wang, Y., Wu, H., & Wu, J. (2011). Tripod measured residual currents and sediment flux: Impacts on the silting of the Deepwater Navigation Channel in the Changjiang estuary. *Estuarine, Coastal and Shelf Science*, 93(3), 192–201. <https://doi.org/10.1016/j.ecss.2010.08.008>
- Luan, H. L., Ding, P.-X., Wang, Z. B., Ge, J.-Z., & Yang, S.-L. (2016). Decadal morphological evolution of the Yangtze Estuary in response to river input changes and estuarine engineering projects. *Geomorphology*, 265, 12–23. <https://doi.org/10.1016/j.geomorph.2016.04.022>
- Manning, A. J., & Dyer, K. R. (2007). Mass settling flux of fine sediments in Northern European estuaries: Measurements and predictions. *Marine Geology*, 245(1–4), 107–122. <https://doi.org/10.1016/j.margeo.2007.07.005>
- Manning, A. J., Langston, W. J., & Jonas, P. J. C. (2010). A review of sediment dynamics in the Severn Estuary: Influence of flocculation. *Marine Pollution Bulletin*, 61(1–3), 37–51. <https://doi.org/10.1016/j.marpolbul.2009.12.012>
- Mellor, G. L., & Yamada, T. (1982). Development of a turbulence closure model for geophysical fluid problem. *Reviews of Geophysics and Space Physics*, 20, 851–875.
- Munk, W. H., & Anderson, E. R. (1948). Notes on the theory of the thermocline. *Journal of Marine Research*, 7, 276–295.
- Pan, L., Ding, P., & Ge, J. (2012). Impacts of Deep Waterway Project on morphological changes within the North Passage of the Changjiang Estuary, China. *Journal of Coastal Research*, 284, 1165–1176. <https://doi.org/10.2112/JCOASTRES-D-11-00129.1>
- Pawlowicz, R., Beardsley, B., & Lentz, S. (2002). Classical tidal harmonic analysis including error estimates in MATLAB using T_TIDE. *Computers and Geosciences*, 28, 929–937.
- Ren, J., & Wu, J. (2014). Sediment trapping by haloclines of a river plume in the Pearl River Estuary. *Continental Shelf Research*, 82(c), 1–8. <https://doi.org/10.1016/j.csr.2014.03.016>
- Restrepo, J. C., Schrottke, K., Traini, C., Bartholomae, A., Ospino, S., Ortíz, J. C., et al. (2018). Estuarine and sediment dynamics in a microtidal tropical estuary of high fluvial discharge: Magdalena River (Colombia, South America). *Marine Geology*, 398, 86–98. <https://doi.org/10.1016/j.margeo.2017.12.008>
- Ross, M. A. (1988). Vertical structure of estuarine fine sediment suspensions, Ph.D. thesis, University of Florida, Gainesville, Florida, USA.
- Shao, Y., Yan, Y., & Maa, J. P.-Y. (2011). In situ measurements of settling velocity near Baimao Shoal in Changjiang Estuary. *Journal of Hydraulic Engineering*, 137(3), 372–380. [https://doi.org/10.1061/\(ASCE\)HY.1943-7900.0000312](https://doi.org/10.1061/(ASCE)HY.1943-7900.0000312)
- Shen, F., & Verhoef, W. (2010). Suppression of local haze variations in MERIS images over turbid coastal waters for retrieval of suspended sediment concentration. *Optics Express*, 18(12), 12,653–12,662. <https://doi.org/10.1364/OE.18.012653>
- Shen, F., Zhou, Y. X., Li, J. F., He, Q., & Verhoef, W. (2013). Remotely sensed variability of the suspended sediment concentration and its response to decreased river discharge in the Yangtze Estuary and adjacent coast. *Continental Shelf Research*, 69, 52–61. <https://doi.org/10.1016/j.csr.2013.09.002>
- Song, D., Wang, X. H., Cao, Z., & Guan, W. (2013). Suspended sediment transport in the Deepwater Navigation Channel, Yangtze River Estuary, China, in the dry season 2009: 1. Observations over spring and neap tidal cycles. *Journal of Geophysical Research: Oceans*, 118, 5555–5567. <https://doi.org/10.1002/jgrc.20410>
- Sottolichio, A., & Castaing, P. (1999). A synthesis on seasonal dynamics of highly-concentrated structures in the Gironde estuary. *Comptes Rendus De l'Académie Des Sciences-Series IIA-Earth and Planetary Science*, 329(11), 795–800.
- Sottolichio, A., Hurther, D., Gratiot, N., & Bretel, P. (2011). Acoustic turbulence measurements of near-bed suspended sediment dynamics in highly turbid waters of a macrotidal estuary. *Continental Shelf Research*, 31(supplement), S36–S49. <https://doi.org/10.1016/j.csr.2011.03.016>
- Stacey, M. T., Brennan, M. L., Bureau, J. R., & Monismith, S. G. (2010). The tidally averaged momentum balance in a partially and periodically stratified estuary. *Journal of Physical Oceanography*, 40(11), 2418–2434. <https://doi.org/10.1175/2010JPO4389.1>
- Tennekes, H., & Lumley, J. L. (1972). *A first course in turbulence*. Cambridge: The MIT Press.
- Toorman, E., Bruens, A., Kranenburg, C., & Winterwerp, J. (2002). Interaction of suspended cohesive sediment and turbulence. *Proceedings in Marine Science*, 5, 7–23.
- Toublanc, F., Brenon, I., Coulombier, T., & Le Moine, O. (2015). Fortnightly tidal asymmetry inversions and perspectives on sediment dynamics in a macrotidal estuary (Charente, France). *Continental Shelf Research*, 1–13. <https://doi.org/10.1016/j.csr.2014.12.009>
- Traykovski, P., Geyer, W. R., Irish, J. D., & Lynch, J. F. (2000). The role of wave-induced density-driven fluid mud flows for cross-shelf transport on the Eel River continental shelf. *Continental Shelf Research*, 20(16), 2113–2140. [https://doi.org/10.1016/S0278-4343\(00\)00071-6](https://doi.org/10.1016/S0278-4343(00)00071-6)
- Traykovski, P., Wiberg, P. L., & Geyer, W. R. (2007). Observations and modeling of wave-supported sediment gravity flows on the Po prodelta and comparison to prior observations from the Eel shelf. *Continental Shelf Research*, 27(3–4), 375–399. <https://doi.org/10.1016/j.csr.2005.07.008>
- Van Maren, D., Winterwerp, J., Wu, B., & Zhou, J. (2009). Modelling hyperconcentrated flow in the Yellow River. *Earth Surface Processes and Landforms*, 34(4), 596–612. <https://doi.org/10.1002/esp.1760>
- Wang, Z. B., & Winterwerp, J. C. (1992). A model to simulate the transport of fluid mud. Tech. Rep. Z163, WL j Delft hydraulics, Delft, the Netherlands. 577, 579.
- Winterwerp, J. (1999). On the dynamics of high-concentrated mud suspensions. Ph.D. thesis, Delft University of Technology.
- Winterwerp, J. (2002). Scaling parameters for high-concentrated mud suspensions in tidal flow. *Proceedings in Marine Science*, 5, 171–186.
- Winterwerp, J. (2006). Stratification effects by fine suspended sediment at low, medium, and very high concentrations. *Journal of Geophysical Research*, 111, C05012. <https://doi.org/10.1029/2005JC003019>
- Winterwerp, J., & Van Kesteren, W. (2004). Introduction to the physics of cohesive sediment in the marine environment, developments in sedimentology 56. Series Editor: T. Van Loon.
- Winterwerp, J. C. (2011). Fine sediment transport by tidal asymmetry in the high-concentrated Ems River: Indications for a regime shift in response to channel deepening. *Ocean Dynamics*, 61(2–3), 203–215. <https://doi.org/10.1007/s10236-010-0332-0>
- Yang, S. L., Milliman, J. D., Li, P., & Xu, K. (2011). 50,000 dams later: Erosion of the Yangtze River and its delta. *Global and Planetary Change*, 75(1–2), 14–20. <https://doi.org/10.1016/j.gloplacha.2010.09.006>